Bachelor's Thesis

# Untersuchung von Quantenverschränkung in off-shell $H^* \to ZZ$ durch Separation von Polarisationszuständen

# Accessing Quantum Entanglement in off-shell $H^* \to ZZ$ with Separation of Polarisation States

prepared by

**Siemen Aulich**

from Emden

at the II. Physikalischen Institut

# Zusammenfassung

Das Higgs-Boson ist das einzige Spin-0-Elementarteilchen im Standardmodell, dessen elektroschwachen Zerfälle ein Paar verschränkter Vektorbosonen produzieren. Die paritätsverletzenden Eigenschaften der elektroschwachen Kopplung der $Z^0$-Bosonen ermöglichen es, ihren Polarisationszustand anhand der leptonischen Zerfallsprodukte zu testen.

Die Cms- und Atlas-Kollaborationen haben vor kurzem den Nachweis für die Produktion von off-shell Higgs im Endzustand von vier Leptonen erbracht. Der Zerfall von off-shell Higgs Bosonen in Vektorbosonen bietet eine geeignete Plattform, die Verschränkung auf der fundamentalsten Ebene zu untersuchen. Der Zerfall in Leptonen ist für eine solche Analyse besonders geeignet, da die kinematischen Variablen der zerfallenden Teilchen mit hoher Präzision aus den Endzustandsteilchen rekonstruiert werden können.

Ein Test der Quantenverschränkung wird formuliert als Suche nach transversalen Polarisationen der $Z^0$-Bosonen in $H^* \to ZZ$ unter Verwendung eines tiefen neuronalen Netzwerks zur Unterscheidung der verschiedenen Polarisationszustände.

**Stichwörter:** Elektroschwache Wechselwirkung, Higgs Boson, Quantenverschränkung, Deep Learning

# Abstract

The Higgs boson is the only spin-0 elementary particle within the Standard Model. Its electroweak decays yield a pair of entangled vector bosons. The parity-violating properties of the electro-weak coupling of the $Z^0$ bosons allow for testing of their polarisation state.

The Cms and Atlas Collaborations recently provided evidence for off-shell Higgs production in the four lepton final state. The decay of the off-shell Higgs to vector bosons offers a great stage to probe entanglement at the most fundamental level. The decay to leptons is particularly suited for such an analysis because the kinematic variables of the decaying particles can be reconstructed with high precision from the final state particles. A test of quantum entanglement is reformulated as a search for transverse polarisations of the $Z^0$ bosons in $H^* \to ZZ$ using a deep neural network to discriminate between the different polarisation states.

**Keywords:** Electroweak Interaction, Higgs boson, Quantum Entanglement, Deep Learning

# Contents

*Contents*

# 1. Introduction

Quantum entanglement is a feature of composite quantum systems where subsystems cannot be described independently of each other. The physicists Einstein, Podolsky and Rosen (EPR) expressed this in a paradox consisting of two entangled particles on which one would perform incompatible measurements. Their Gedankenexperiment stated that performing these measurements and the resulting collapse of the wave function of the entangled system would violate the principle of locality and allow for information transport faster than the speed of light. To counter this problem, a local real theory with hidden parameters that predetermined the outcome of the measurement was proposed. Quantum entanglement is one of the most distinct properties that separates classical from quantum mechanics. Nevertheless, it remained uncertain how entanglement might be investigated in an experiment. In recent decades, different experiments have been searching for evidence of quantum entanglement in various systems.

The discovery of the Higgs boson by the ATLAS and CMS Collaborations in the year 2012 was a major breakthrough in particle physics. The Higgs boson is a central piece in the Standard Model and was predicted almost 60 years before its discovery. Its interaction properties are crucial for humanity's understanding of the most fundamental processes of our universe.

Continuously testing and questioning the models humans use to describe nature is important for scientific advance. Thus, it is important to see if the rules that govern quantum mechanics apply regardless of the scale at which they are tested.

This work aims at testing if entanglement can be observed in the decay of an off-shell Higgs boson to $Z^0$ vector bosons. The decay channel $H^* \to ZZ \to 4\ell$ is particularly suited for such an analysis because charged leptons allow for a precise measurement of their kinematic variables and efficient particle identification. Due to the flavour conversation and $Z^0$ on-shell condition a precise reconstruction of the $Z^0$ kinematics becomes possible.

This work starts with a brief overview of the Standard Model of particle physics, the theoretical framework describing the interaction of fundamental particles. This is followed by a description of quantum entanglement and its appearance in the $gg \to H^* \to ZZ$

process. Afterwards, the experimental setup, consisting of the Lʜᴄ and Aᴛʟᴀs detector is presented. The following chapter is dedicated to event generation in general and the event generation employed in this work to model this specific process. The event selection and analysis strategy that was used in this work is featured in Chapter 5. An assessment of the event selection and the presentation of the result of the fitting procedure is done in Chapter 6. The last chapter concludes the work done in this thesis and gives an outlook into further research possibilities.

# 2. Theory

## 2.1. The Standard Model of Particle Physics

### 2.1.1. Overview

The Standard Model of particle physics (SM) is the state-of-the-art theoretical framework to describe the known particles and three of the four fundamental forces as the interactions between these particles. The Higgs mechanism was the latest addition to the SM and was introduced to account for the particle masses [2–7]. The SM is a renormalisable quantum field theory and therefore predicts finite cross-sections. The structure of the theory can be explained using the Lagrangian which gives rise to the properties of the particles and their interactions with each other [8–20]. However, it shall be noted that the Lagrangian does not account for the quantization of the theory.

As depicted in Figure 2.1, elementary particles of three types of spin occur. Those with spin $S = \frac{1}{2}$ are called fermions, those with $S = 0/1$ are called bosons. The Standard Model has five gauge bosons with spin $S = 1$ and the Higgs boson with $S = 0$.

Three types of interaction exist within the Standard Model with each particle differing in the way it participates in these interactions. The colour charge is responsible for the strong interaction of particles, electric charge $Q$ for the electromagnetic interaction. The fermions can be divided into quarks and leptons. Quarks are colour-charged while leptons are not. The particles are arranged as three generations of matter, where the particle masses increase with each generation. Every fermion exists as a particle and as an antiparticle. The antiparticle only differs in the additive quantum numbers such as an oppositely signed electric charge. Two left-handed leptons or two left-handed quarks of the same generation form a weak isospin doublet. The charge of two particles in one weak isospin doublet differs by $1e$. The right-handed particles each form a weak isospin singlet with the third component of weak isospin $I_3 = 0$. For quarks, the up-type quark has an electric charge of $Q = +\frac{2}{3}$ and a third component of the weak isospin $I_3 = +\frac{1}{2}$ and the down-type quark $Q = -\frac{1}{3}$ and $I_3 = -\frac{1}{2}$. For leptons, each weak isospin doublet consists of a particle with electric charge $Q = -1$ and the third component of weak isospin $I_3 = -\frac{1}{2}$
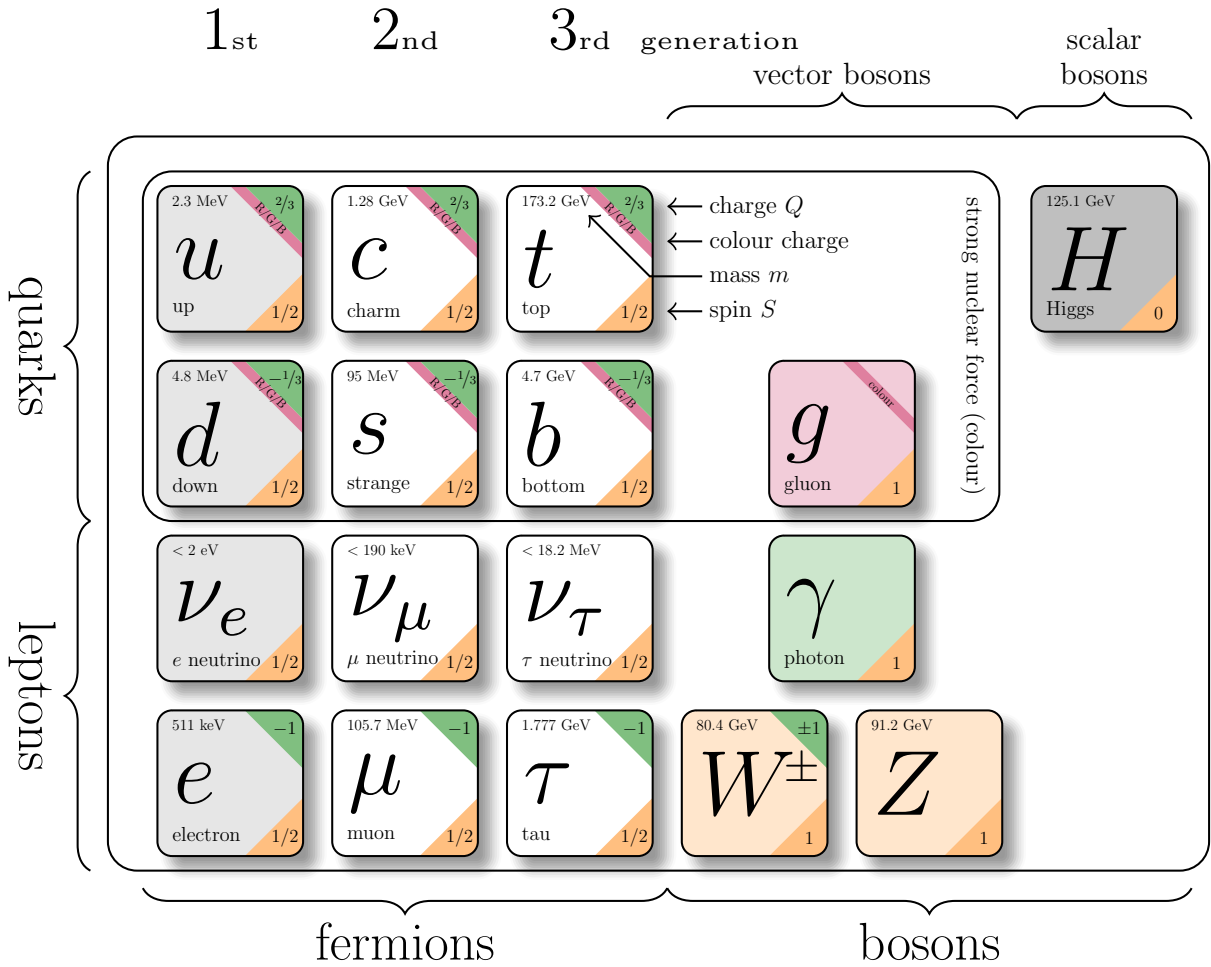
**Figure 2.1.:** Particles of the Standard Model of particle physics. The figure was created using data from [1].

and a corresponding neutrino with electric charge $Q = 0$ and $I_3 = +\frac{1}{2}$.

There are five gauge bosons. The massless photon mediates the electromagnetic interaction. The massless gluon mediates the strong interaction. The three massive $W^\pm, Z^0$ bosons mediate the weak interaction. Gravitation as the fourth fundamental force is not included in the SM.

## 2.1.2. The Strong Interaction (QCD)

Quantum chromodynamics (QCD) describes the strong interaction as the coupling of colour-charged particles to the gluon. This coupling gives rise to the local SU(3) gauge symmetry [25, 26]. Only the quarks and the gluon itself are colour-charged and thus couple to the gluon field. Due to the non commuting structure of the SU(3) group, gluons engage in self-interactions. The colour-charged particles are subject to the confinement
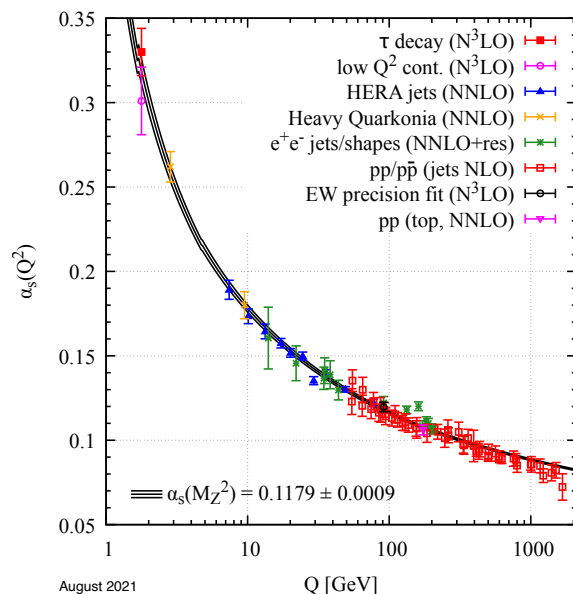
*Figure 2.2.:* Summary of measurements of $\alpha_S$ as a function of the energy scale $Q$. The Measurements were performed by various groups [21–24]. The figure is taken from [1].

[27], which describes that colour-charged particles always appear in neutral colour-charged bound states. This may be understood by the effective potential [28]

$$V(r) = -\frac{\kappa}{r} + \frac{r}{a^2} \, , \tag{2.1}$$

with $\kappa$ a constant related to the coupling strength of QCD, $r$ the distance between quark and anti-quark and $\frac{1}{a^2}$ a constant describing the strength of the linear term. This potential leads to increasing potential energy as quark and anti-quark are separated and thus the creation of new quarks which form hadrons.

The coupling constant of the strong interaction depends on the energy scale of the interaction. One important feature of this energy dependence is the asymptotic freedom [29] which refers to a decreasing coupling constant for high energy. The energy dependence of the coupling constant is shown in Figure 2.2.

## 2.1.3. The Electroweak Interaction

The electromagnetic and weak interaction can be understood as corresponding to the same gauge symmetry. The spontaneous symmetry breaking associated with the Higgs mechanism explains how the different fields come into existence [8–12]. Quantum electrodynamics (QED) describes the coupling of electric charged particles to the photon field

corresponding to the $U(1)$ symmetry [30–37].

The weak interaction is mediated by three bosons $W^\pm$ and $Z^0$. These bosons correspond to the $\mathrm{SU}(2)_L$ symmetry. The subscript $L$ refers to the exclusive action on the left-handed particles of the symmetry operation. The action of this symmetry group on the right-handed singlets is trivial. These bosons are massive through their coupling to the Higgs field. The $W^\pm$ both have the same mass, a weak isospin of $I_3 = \pm 1$, and an electric charge of $Q = \pm 1$. The $Z^0$ has a different mass and vanishing weak isospin and electric charge.

The weak charged current interaction is the coupling of particles to the $W^\pm$ bosons. The $W^\pm$ bosons couple exclusively to left-handed particles. This property is expressed by the vertex factor for the weak interaction of leptons [10–12]

$$i\frac{g_w}{2\sqrt{2}}\gamma^\mu(1 - \gamma^5) \, , \qquad (2.2)$$

as the $1 - \gamma^5$ term which projects a spinor on its left-handed component. Experimental evidence for this property was first found in the Wu-experiment [38].

For the coupling of quarks to the $W^\pm$ bosons one has to consider the CKM-matrix [39, 40], giving the vertex factor

$$i\frac{g_w}{2\sqrt{2}}\gamma^\mu(1 - \gamma^5)V_{ij} \, . \qquad (2.3)$$

The matrix elements $V_{ij}$ account for the transition from mass to flavour eigenstates of the quarks. The modulus of these matrix elements is largest for diagonal elements, corresponding to interactions within one particle generation.

The weak neutral current is the coupling of particles to the $Z^0$ bosons. Unlike the $W^\pm$ bosons, the $Z^0$ does not couple exclusively to left-handed particles but to left- and right-handed particles in a different manner. The vertex factor is given by [9]

$$i\frac{g_z}{2}\gamma^\mu(2Q\sin^2(\theta_W) + I_3(1 - \gamma^5)) \, , \qquad (2.4)$$

where $\theta_W$ is the Weinberg mixing angle. From the vertex factor, it can be inferred that the $Z^0$ boson can couple to right-handed charged particles. Further, it is noteworthy that the $Z^0$ bosons coupling lacks the flavour mixing properties of the $W^\pm$ bosons.

### 2.1.4. The Higgs Mechanism

The Higgs mechanism describes how gauge bosons acquire their mass since mass terms in the Lagrangian conflict with the gauge invariance. To avoid this, another field with a non-

vanishing vacuum expectation value is introduced [2–4]. For the electroweak interaction, this can be explained by the introduction of a doublet of complex scalar fields [9, 41]

$$\phi = \begin{pmatrix} \phi^+ \\ \phi^0 \end{pmatrix} = \frac{1}{\sqrt{2}} \begin{pmatrix} \phi_1 + i\phi_2 \\ \phi_3 + i\phi_4 \end{pmatrix}. \tag{2.5}$$

Further, a potential term of the form [9]

$$V(\phi) = -\mu^2(\phi^\dagger \phi) + \lambda(\phi^\dagger \phi)^2 \tag{2.6}$$

is added to the Lagrangian. Where $\mu^2, \lambda$ are positive real constants. This potential takes its minimal value for $\langle 0 | \phi | 0 \rangle = \sqrt{\frac{\mu^2}{2\lambda}} \neq 0$ which corresponds to the non-vanishing vacuum expectation value for the Higgs field.

Enforcing local gauge invariance under $\mathrm{SU}(2)_L \times \mathrm{U}(1)_Y$ yields the masses of the corresponding bosons. The physical fields $W^\pm, Z^0, \gamma$ appear as linear combinations of the $W^i, B$ gauge fields. This process explains the different interaction properties of these fields. The linear combination can be denoted as [8]

$$W_\mu^\pm = \frac{1}{\sqrt{2}}(W_\mu^1 \pm i W_\mu^2) \tag{2.7}$$

$$Z_\mu = -\sin(\theta_W)B_\mu + \cos(\theta_W)W_\mu^3 \tag{2.8}$$

$$A_\mu = \cos(\theta_W)B_\mu + \sin(\theta_W)W_\mu^3. \tag{2.9}$$

Their masses can be parametrised as

$$m_W = \frac{1}{2}g_W v \tag{2.10}$$

$$m_Z = \frac{1}{2}v\frac{g_W^2}{\cos(\theta_W)} \tag{2.11}$$

$$m_A = 0 \tag{2.12}$$

where $g_W$ is the coupling constant of $\mathrm{SU}(2)_L$ gauge field, and $v = \sqrt{\frac{\mu^2}{\lambda}} \approx 246\,\mathrm{GeV}$ is the vacuum expectation value of the Higgs field [1].

The introduction of the scalar field into the Lagrangian also yields the Higgs boson as the excitation of the Higgs field from its vacuum value. Further, it generates coupling terms in the Lagrangian which correspond to interactions between the $W^\pm$ and $Z^0$ bosons and the Higgs boson as depicted in Figure 2.3. The mass of the Higgs boson itself is given as

$$m_H = \sqrt{2\lambda v^2}. \tag{2.13}$$
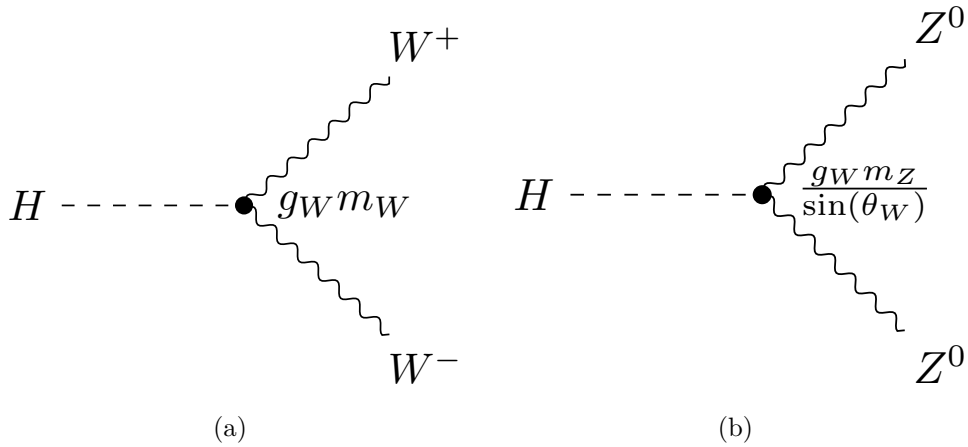
***Figure 2.3.:*** Interaction vertices for the coupling of the Higgs boson to the (a) $W$ boson; (b) $Z^0$ bosons.

Furthermore, the Higgs mechanism also predicts three- and four-point self-interactions of the Higgs boson.

The mass of the fermions can be described by the Yukawa coupling of the fermions to the Higgs field [9]. To do so, a term of the form

$$\mathcal{L}_m = -g_f \left[ \bar{f}_L \phi f_R + \bar{f}_R \bar{\phi} f_L \right] \tag{2.14}$$

is introduced for every fermion. The factor $g_f$ is the coupling strength of the fermion to the Higgs field. This yields the masses of the fermions as

$$m_f = \frac{g_f v}{\sqrt{2}}. \tag{2.15}$$

The Yukawa-coupling also implies interaction vertices of fermions to the Higgs boson.

## 2.1.5. Higgs Boson Production and Decay

The SM predicts different mechanisms for the production of the Higgs boson. For a *pp*-collider such as the LHC, the most dominant process is the gluon-gluon fusion (ggF) where two gluons initiate a virtual quark loop which produces the Higgs boson. The production of a Higgs boson is mediated by a top/bottom quark loop since it is the most massive quark and thus couples strongest to the Higgs boson.

In vector boson fusion (VBF), two quarks radiate a $W^+W^-$ or $ZZ$ pair which couple to the Higgs boson. Higgs Strahlung ($WH$ and $ZH$) describes the process of coupling a fermion and antifermion to a $W^\pm$ or $Z^0$ boson which radiates a Higgs boson. Associated

| Production mode | Cross section in pb |
|:---:|:---:|
| ggF | $48.6^{+5.6\%}_{-7.4\%}$ |
| VBF | $3.78^{+2.1\%}_{-2.1\%}$ |
| $WH$ | $1.37^{+2.0\%}_{-2.0\%}$ |
| $ZH$ | $0.88^{+4.1\%}_{-3.5\%}$ |
| $t\bar{t}H$ | $0.50^{+6.8\%}_{-9.9\%}$ |
| total | 55.1 |

**Table 2.1.:** Cross section for different Higgs production modes at $\sqrt{s} = 13\,\text{TeV}$ for $m_H = 125\,\text{GeV}$ [1]. The sub- and superscripted values are the relative uncertainties of each value.

| Decay channel | Branching ratio in % |
|:---:|:---:|
| $H \to b\bar{b}$ | $58.2^{+1.2\%}_{-1.3\%}$ |
| $H \to W^+W^-$ | $21.4^{+1.5\%}_{-1.5\%}$ |
| $H \to \tau^+\tau^-$ | $6.27^{+1.6\%}_{-1.6\%}$ |
| $H \to c\bar{c}$ | $2.89^{+5.5\%}_{-2.0\%}$ |
| $H \to ZZ$ | $2.62^{+1.5\%}_{-1.5\%}$ |
| $H \to \gamma\gamma$ | $0.227^{+2.1\%}_{-2.1\%}$ |
| $H \to Z\gamma$ | $0.153^{+5.8\%}_{-5.8\%}$ |
| $H \to \mu^+\mu^-$ | $0.0218^{+1.7\%}_{-1.7\%}$ |

**Table 2.2.:** Branching ratio for different decay channels of the Higgs boson [1]. The sub- and superscripted values are the relative uncertainties of each value. Note that these are the branching ratios of the on-shell Higgs decay. These values differ for the case of an off-shell Higgs due to the phase space that is available in the decay.

production with a top quark pair ($ttH$) refers to the coupling of two gluons to a $t\bar{t}$ pair and subsequent coupling of a top- or antitopquark to a Higgs boson. This process is favoured with respect to other quarks, due to the top quark's large mass and Yukawa coupling. The Feynman diagrams for these processes are depicted in Figure 2.4.

Predictions for the cross section of the different Higgs production modes are shown in Table 2.1.

Due to its large mass, the Higgs boson decays quickly via different channels. The predicted branching ratios for different decay channels are given in Table 2.2.

The ATLAS and CMS collaborations both reported the observation of a new boson with the properties the SM predicted for the Higgs boson and a mass of $m_H = 125\,\text{GeV}$ [42, 43].

The SM predicted the spin of the Higgs boson to be $S = 0$. This is supported by observations of the Higgs at the LHC excluding of the $S = 2$ hypothesis [44]. The parity
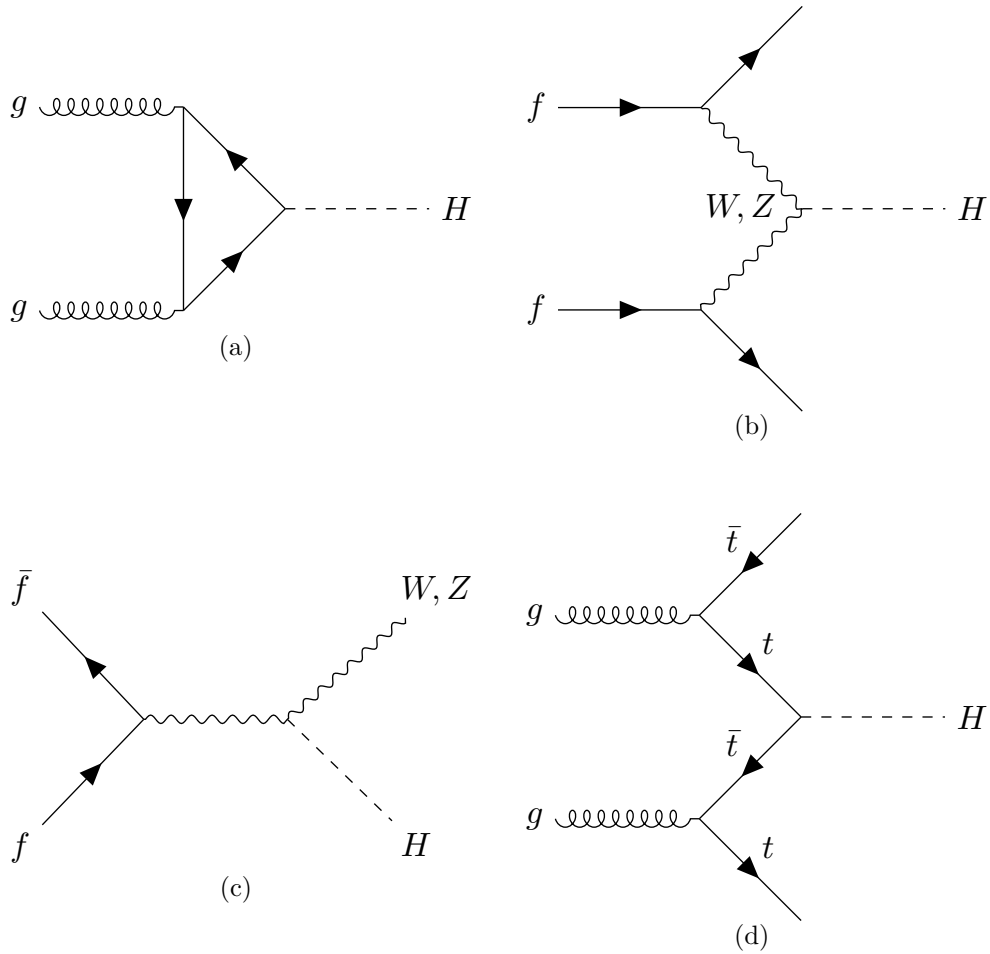
***Figure 2.4.:*** Feynman diagrams for the leading order processes of the Higgs production (a) gluon fusion(ggF), (b) vector boson fusion(VBF), (c) Higgs Strahlung (WH and ZH); and, (d) top fusion (ttH) at the LHC at $\sqrt{s} = 13\,\text{TeV}$ [1].

of the Higgs boson was further observed to be positive.

## 2.1.6. $H^* \to ZZ \to 4\ell$

| Decay channel | Branching ratio in % |
|---|---|
| $Z \to q\bar{q}$ | $69.967 \pm 0.093$ |
| $Z \to e^+e^-$ | $3.3632 \pm 0.0042$ |
| $Z \to \mu^+\mu^-$ | $3.662 \pm 0.0066$ |
| $Z \to \tau^+\tau^-$ | $3.6696 \pm 0.0083$ |
| invisible | $19.934 \pm 0.098$ |

***Table 2.3.:*** Branching ratio measurements for the $Z^0$ boson decay [45].

The $Z^0$ boson has a mass of $m_Z = 91.1875 \pm 0.0021\,\text{GeV}$ [1]. With the Higgs bosons' mass being $m_H = 125\,\text{GeV}$, it has to be off-shell to decay into two on-shell $Z^0$ bosons. The branching ratios for the on-shell Higgs decay of the $Z^0$ boson decay are given in Table 2.3. One can see that both $Z^0$ bosons can further decay to leptons. These decays are of particular interest since $\mu^\pm$ and $e^\pm$ are well suited for a precise measurement of the kinematic variable in the detector. Since the decay of the $Z^0$ bosons contains the leptonic flavour, the decay $H^* \to ZZ \to 4\ell$ allows for a precise reconstruction of the $Z^0$ bosons' kinematics. To assess the number of events the cross section of the $gg \to H^* \to ZZ \to 4\ell$ with $\ell = \mu, e$ is calculated.

The cross section is computed at next to leading order using MADGRAPH. At a centre of mass energy of $\sqrt{s} = 13\,\text{TeV}$ it is given by $\sigma = 0.0002571\,\text{pb}$. Neglecting any detection or reconstruction inefficiencies the expected number of events can be calculated as

$$N = \sigma \cdot \mathcal{L}\,. \tag{2.16}$$

Here $\mathcal{L}$ refers to the integrated luminosity. With the integrated luminosity $\mathcal{L} \approx 140\,\text{fb}^{-1}$ the expected number of events amounts to $N \approx 71.988$. For the High-Luminosity Large Hadron Collider with $\mathcal{L} \approx 3\,\text{ab}^{-1}$, it increases to $N \approx 1,542.600$.

## 2.2. Entanglement

Entanglement refers to the inseparability of a state in a tensor product Hilbert space. A tensor product Hilbert space usually corresponds to a system made up of multiple particles. If a multi-particle system's state is not separable, the particles can not be described independently. Acting on one particle also changes the other particles' states. Consider a tensor product Hilbert space $\mathcal{H} = \mathcal{H}_A \otimes \mathcal{H}_B$. A state $|\psi\rangle \in \mathcal{H}$ is separable if

$$|\psi\rangle = |\phi\rangle_A \otimes |\varphi\rangle_B \qquad\qquad |\phi\rangle_A \in \mathcal{H}_A, |\varphi\rangle_B \in \mathcal{H}_B\,. \tag{2.17}$$

A density matrix is separable if

$$\rho = \sum_i w_i \rho_{A,i} \otimes \rho_{B,i}\,. \tag{2.18}$$

For the most general case of a Hilbert space, no test for entanglement is known. However, the Peres-Horodecki criterion [46, 47] provides a sufficient condition for entanglement. For certain cases of limited dimensionality, the Peres-Horodecki criterion also becomes a necessary condition. Generically this is only the case if we assume without loss of

generality $\dim(\mathcal{H}_A) \leq 2$ and $\dim(\mathcal{H}_B) \leq 3$ but also for the case of the two $Z^0$ bosons in Higgs decays [48].

## 2.2.1. Entanglement in the $H^* \to ZZ \to 4\ell$ Decay Mode
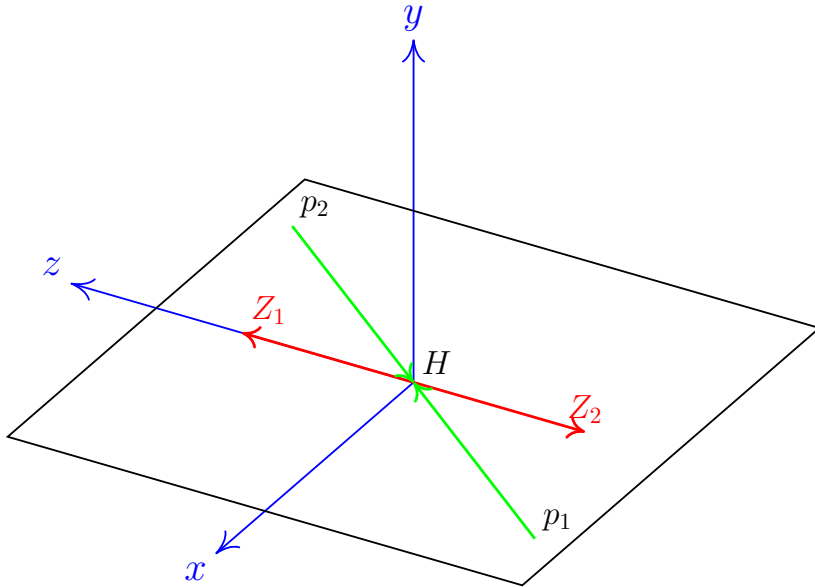


**Figure 2.5.:** Depiction of the reference system used in this analysis.

Consider the two $Z^0$ bosons in the Higgs boson's centre of mass reference frame. Here and in the following, the $z$-axis is chosen such that it aligns with the $Z^0$ bosons three momentum. The $x$-axis is in the plane spanned by the incoming protons and the $Z^0$ bosons. The $y$-axis is taken to be $\hat{y} = \hat{z} \times \hat{x}$. This choice of reference system is similar to the one in [48, 49]. A graphical depiction of this choice of reference system is given in Figure 2.5. The eigenstate of the third component of the spin will be denoted as $|-\rangle, |0\rangle, |+\rangle$. Since the Higgs boson is a scalar particle, the only non-vanishing elements of the density matrix $\rho$ of the spins of the two $Z^0$ bosons are

$$\langle u_i | \rho | u_j \rangle \,, \tag{2.19}$$

where $|u_1\rangle = |+-\rangle, |u_2\rangle = |-+\rangle, |u_3\rangle = |00\rangle$.

Thus the density matrix may be written as a linear combination [48]

$$\rho = \sum p_l |l\rangle \langle l| \quad p_l \geq 0, \ \sum_l p_l = 1 \,, \tag{2.20}$$

where

$$|l\rangle = \alpha_1 |+-\rangle + \alpha_2 |00\rangle + \alpha_3 |-+\rangle \quad \sum_i |\alpha_i|^2 = 1 \,. \tag{2.21}$$

Due to the conservation of parity in the $H \to ZZ$ process for a particular event, the $Z^0$ bosons spin state can be considered as

$$|\psi\rangle = \frac{1}{\sqrt{2 + \beta^2}} (|-+\rangle - \beta |00\rangle + |+-\rangle) \,. \tag{2.22}$$

For the coefficient $\beta$ one can find [48]

$$\beta = 1 + \frac{m_H^2 - (m_{Z_1} + m_{Z_2})^2}{2 m_{Z_1} m_{Z_2}} \,. \tag{2.23}$$

To obtain the density matrix for an ensemble of possible values for the $m_{Z_1}, m_{Z_2}$ an integration over the phase space has to be performed. The dependence on chirality in the weak decays allows for a reconstruction of the density matrix of the $Z^0$ bosons using the distribution of the kinematic variables of the leptonic decay products. The density matrix itself has 81 terms, due to the dimension of the tensor product Hilbert space being 9. Another component of the density matrix is fixed by the normalisation condition $\mathrm{Tr}(\rho) = 1$.

However, the form of the density matrix is constrained, since only 9 out of the 80 possible terms are non-vanishing [48].

$$\rho = \frac{1}{2c + w^2} \begin{pmatrix} 0 & 0 & 0 & 0 & 0 & 0 & 0 & 0 & 0 \\ 0 & 0 & 0 & 0 & 0 & 0 & 0 & 0 & 0 \\ 0 & 0 & c & 0 & -y & 0 & c & 0 & 0 \\ 0 & 0 & 0 & 0 & 0 & 0 & 0 & 0 & 0 \\ 0 & 0 & -y & 0 & w^2 & 0 & -y & 0 & 0 \\ 0 & 0 & 0 & 0 & 0 & 0 & 0 & 0 & 0 \\ 0 & 0 & c & 0 & -y & 0 & c & 0 & 0 \\ 0 & 0 & 0 & 0 & 0 & 0 & 0 & 0 & 0 \\ 0 & 0 & 0 & 0 & 0 & 0 & 0 & 0 & 0 \end{pmatrix} \tag{2.24}$$

Note, that the form of the state in Equation 2.22 fixes $c = 1$. It is, however, left as a variable, since it allows to denote the condition for entanglement of this system in a concise manner.

*2. Theory*

The coefficients $w, y$ are obtained via an integration over the phase space [48]

$$\rho = \int \rho_\beta \cdot \mathcal{P}(\beta) \, d\beta \,,$$
$$\rho_\beta = |\psi\rangle \langle\psi| \,, \tag{2.25}$$

where $\mathcal{P}(\beta)$ is the probability density function of the kinematic variable $\beta$. The state $|\psi\rangle$ is given in Equation 2.22.

In the $H^* \to ZZ$ process, the two masses $m_{Z_{1,2}}$ in Eq. 2.23 are fixed by the condition that both $Z^0$ are on-shell. The mass $m_H$, however, is variable and it is evident that for increasing values of $m_H$ the contribution of the transverse polarisation diminishes. Thus, the state becomes primarily longitudinal polarised. Therefore, the form of the density matrix and especially the off-diagonal elements depends on the cuts applied to the system.

Note that the derivation in [48] was done for the case of an on-shell Higgs but is nonetheless applicable here. Since, the Higgs coupling to $Z^0$ bosons does not change for off-shell Higgs. The constraint form of the density matrix ensures that the condition for entanglement in this matrix is equivalent to any non-vanishing off-diagonal elements [48]. The condition for entanglement can be more explicitly expressed as

$$y \neq 0 \vee c \neq 0 \,. \tag{2.26}$$

## 2.2.2. Decay of Polarised $Z^0$ Bosons

Due to the chiral-dependent nature of the $Z^0$ boson coupling, the decay amplitude of the $Z^0$ boson is dependent on its spin. This can be expressed via the decay density matrix of the $Z^0$ boson. It contains the angular decay distribution for the corresponding spin states of the $Z^0$ boson. For the case of the $Z^0$ boson, it is given by [50]

$$\Gamma = \frac{1}{4} \begin{pmatrix} 1 + \cos^2(\theta) + 2\eta_\ell \cos(\theta) & \frac{1}{\sqrt{2}}(\sin(2\theta) - 2\eta_\ell \sin(\theta))e^{i\varphi} & (1 - \cos^2(\theta))e^{i2\varphi} \\ \frac{1}{\sqrt{2}}(\sin(2\theta) - 2\eta_\ell \sin(\theta))e^{-i\varphi} & 2\sin^2(\theta) & -\frac{1}{\sqrt{2}}(\sin(2\theta) + 2\eta_\ell \sin(\theta))e^{i\varphi} \\ (1 - \cos^2(\theta))e^{-2i\varphi} & -\frac{1}{\sqrt{2}}(\sin(2\theta) + 2\eta_\ell \sin(\theta))e^{-i\varphi} & 1 + \cos^2(\theta) - 2\eta_\ell \cos(\theta) \end{pmatrix} \tag{2.27}$$

where

$$\eta_\ell = \frac{1 - \sin^2(\theta_W)}{1 - 4\sin^2(\theta_W) + 8\sin^4(\theta_W)} \,. \tag{2.28}$$

The angles $\theta, \varphi$ are the azimuthal and polar angle of the negative lepton in the $Z^0$ bosons centre-of-mass frame. The decay amplitude of a certain spin state $|\psi\rangle$ can be evaluated as

$$\frac{1}{\sigma}\frac{d\sigma}{d\Omega} = \langle\psi|\,\Gamma\,|\psi\rangle\,. \tag{2.29}$$

For a mixed state, the decay amplitude can be computed as

$$\frac{1}{\sigma}\frac{d\sigma}{d\Omega} = \text{Tr}\,(\rho\cdot\Gamma)\,. \tag{2.30}$$

Two notable cases for the spin state of the $Z^0$ shall be discussed here. First the case of longitudinally polarized $Z^0$ boson. Its differential cross-section simply reads

$$\frac{1}{\sigma}\frac{d\sigma}{d\Omega} = \langle 0|\,\Gamma\,|0\rangle = \frac{1}{2}\sin^2(\theta)\,. \tag{2.31}$$

Now consider the case of two transverse polarised $Z^0$ bosons originating from a Higgs decay. Their spin state can be denoted as [48]

$$|\psi\rangle = \frac{1}{\sqrt{2}}\left(|+-\rangle + |-+\rangle\right)\,. \tag{2.32}$$

The state of each $Z^0$ boson can be described as a pure state. It is, however, described by the density matrix

$$\rho_1 = \frac{1}{\sqrt{2}}\left(|+\rangle\,\langle+| + |-\rangle\,\langle-|\right)\,. \tag{2.33}$$

Using this state and Eq. 2.30 the differential cross section is given by

$$\frac{1}{\sigma}\frac{d\sigma}{d\Omega} = \text{Tr}(\rho_1\cdot\Gamma) = \text{Tr}\begin{pmatrix} 1+\cos^2(\theta)+2\eta_\ell\cos(\theta) & 0 & 0 \\ 0 & 0 & 0 \\ 0 & 0 & 1+\cos^2(\theta)-2\eta_\ell\cos(\theta) \end{pmatrix} \tag{2.34}$$
$$= \frac{1}{2}\left(1+\cos^2(\theta)\right)\,.$$

The differential cross section of the $ZZ \to 4\ell$ process can for a mixed state of the $ZZ$ system be written as [48]

$$\frac{1}{\sigma}\frac{d\sigma}{d\Omega_1 d\Omega_2} = \left(\frac{3}{4\pi}\right)^2 \text{Tr}\left(\rho\cdot(\Gamma_1\otimes\Gamma_2)^T\right)\,. \tag{2.35}$$

*2. Theory*

Taking advantage of the constraint form of the density matrix of the $ZZ$ system as in Chapter 2.2.1, one can decompose it into three separate parts

$$\rho_{ZZ} = \rho_{LL} + \rho_{TT} + \rho_{LT}. \tag{2.36}$$

The three matrices are given as

$$\rho_{LL} = \frac{1}{2c + w^2} \begin{pmatrix} 0 & 0 & 0 & 0 & 0 & 0 & 0 & 0 & 0 \\ 0 & 0 & 0 & 0 & 0 & 0 & 0 & 0 & 0 \\ 0 & 0 & 0 & 0 & 0 & 0 & 0 & 0 & 0 \\ 0 & 0 & 0 & 0 & 0 & 0 & 0 & 0 & 0 \\ 0 & 0 & 0 & 0 & w^2 & 0 & 0 & 0 & 0 \\ 0 & 0 & 0 & 0 & 0 & 0 & 0 & 0 & 0 \\ 0 & 0 & 0 & 0 & 0 & 0 & 0 & 0 & 0 \\ 0 & 0 & 0 & 0 & 0 & 0 & 0 & 0 & 0 \\ 0 & 0 & 0 & 0 & 0 & 0 & 0 & 0 & 0 \end{pmatrix}, \tag{2.37}$$

$$\rho_{TT} = \frac{1}{2c + w^2} \begin{pmatrix} 0 & 0 & 0 & 0 & 0 & 0 & 0 & 0 & 0 \\ 0 & 0 & 0 & 0 & 0 & 0 & 0 & 0 & 0 \\ 0 & 0 & c & 0 & 0 & 0 & c & 0 & 0 \\ 0 & 0 & 0 & 0 & 0 & 0 & 0 & 0 & 0 \\ 0 & 0 & 0 & 0 & 0 & 0 & 0 & 0 & 0 \\ 0 & 0 & 0 & 0 & 0 & 0 & 0 & 0 & 0 \\ 0 & 0 & c & 0 & 0 & 0 & c & 0 & 0 \\ 0 & 0 & 0 & 0 & 0 & 0 & 0 & 0 & 0 \\ 0 & 0 & 0 & 0 & 0 & 0 & 0 & 0 & 0 \end{pmatrix}, \tag{2.38}$$

$$\rho_{LT} = \frac{1}{2c + w^2} \begin{pmatrix} 0 & 0 & 0 & 0 & 0 & 0 & 0 & 0 & 0 \\ 0 & 0 & 0 & 0 & 0 & 0 & 0 & 0 & 0 \\ 0 & 0 & 0 & 0 & -y & 0 & 0 & 0 & 0 \\ 0 & 0 & 0 & 0 & 0 & 0 & 0 & 0 & 0 \\ 0 & 0 & -y & 0 & 0 & 0 & -y & 0 & 0 \\ 0 & 0 & 0 & 0 & 0 & 0 & 0 & 0 & 0 \\ 0 & 0 & 0 & 0 & -y & 0 & 0 & 0 & 0 \\ 0 & 0 & 0 & 0 & 0 & 0 & 0 & 0 & 0 \\ 0 & 0 & 0 & 0 & 0 & 0 & 0 & 0 & 0 \end{pmatrix}. \tag{2.39}$$

Here $\rho_{LL}$ is the density matrix corresponding to the longitudinal polarisations of the $ZZ$ system, $\rho_{TT}$ corresponds to the transverse polarisation and $\rho_{LT}$ to the remaining off-

diagonal elements. Note that the $\rho_{TT}$ part also contains off-diagonal elements. Using the linearity of the trace, the differential cross section can be written as

$$\frac{d\sigma}{d\Omega_1 d\Omega_2}(ZZ) = \mu_{LL}\frac{d\sigma}{d\Omega_1 d\Omega_2}(Z_L Z_L) + \mu_{QE}\left(\frac{d\sigma}{d\Omega_1 d\Omega_2}(Z_T Z_T) + \frac{d\sigma}{d\Omega_1 d\Omega_2}(Z_L Z_T)\right).$$

(2.40)

The norm factor is fixed to $\mu_{QE} = 1$, but is added for convenience. The amplitudes are related to density matrices in the form of

$$\frac{d\sigma}{d\Omega_1 d\Omega_2}(Z_L Z_L) \propto \mathrm{Tr}(\rho_{LL} \cdot \Gamma), \tag{2.41}$$

$$\frac{d\sigma}{d\Omega_1 d\Omega_2}(Z_T Z_T) \propto \mathrm{Tr}(\rho_{TT} \cdot \Gamma), \tag{2.42}$$

$$\frac{d\sigma}{d\Omega_1 d\Omega_2}(Z_L Z_T) \propto \mathrm{Tr}(\rho_{LT} \cdot \Gamma). \tag{2.43}$$

The decay density matrix accounts for the angular distribution of the decay products and not for the total cross section. Thus, the amplitudes are only determined up to a proportionality constant.

Note, that the matrices $\rho_{TT}$ and $\rho_{LT}$ are proportional to the factors $c, y$. From this relation it follows that the condition for entanglement in Equation 2.26 is equivalent to any non-vanishing amplitudes from components other than $\frac{d\sigma}{d\Omega_1 d\Omega_2}(Z_L Z_L)$ [51].

The condition for entanglement can be turned into a binary test between two hypotheses:

1. (Separable): The $ZZ$ systems' state is made up of only longitudinally polarised $Z^0$ bosons. This corresponds to $\mu_{QE} = 0$.

2. (Entangled): The $ZZ$ systems' state contains other polarisation contributing to the decay amplitude. This corresponds to $\mu_{QE} \neq 0$.

# 3. Experimental Setup

## 3.1. The LHC

The Large Hadron Collider (LHC) at CERN is a synchrotron designed to accelerate protons and lead nuclei. This work focuses on the proton-proton collisions during Run 2. During Run 2 from 2015 to 2018, the LHC operated at a centre of mass energy of $\sqrt{s} = 13\,\text{TeV}$ with an integrated luminosity of $\mathcal{L}_{int} \approx 140\,\text{fb}^{-1}$ [52].
After completion of Run 3 in Dec. 2025 and an operational pause, the LHC will operate with increased luminosity as the High-Luminosity Large Hadron Collider (HL-LHC). During this phase, it is planned to accumulate data with an integrated luminosity of $\mathcal{L} = 3\,\text{ab}^{-1}$ [53].

## 3.2. The Detector

The ATLAS detector is a general-purpose particle detector at the LHC at CERN. It can roughly be separated into three elements: the inner detector, the calorimeter and the muon spectrometer [54].

### 3.2.1. The Coordinate System

The interaction point marks the origin of the ATLAS coordinate system. The $z$-axis is orientated along the beamline, the $x$-axis points towards the centre of the LHC and the $y$-axis points upwards.
Using this convention several kinematic variables are defined. One of which is the transverse momentum defined as

$$p_T = \sqrt{p_x^2 + p_y^2} \tag{3.1}$$

Because of the cylindrical shape of the ATLAS detector and the cylindrical symmetry of the interactions, the azimuthal angle is used as another variable. The polar angle relative

to the $z$-axis can be used to define the pseudorapidity which can also be expressed in terms of the momentum

$$\eta = -\ln\left(\tan\left(\frac{\theta}{2}\right)\right) = \ln\left(\frac{|\vec{p}| + p_z}{|\vec{p}| - p_z}\right). \tag{3.2}$$

In the ultra-relativistic limit $m \ll |\vec{p}|$ the pseudorapidity is equal to the rapidity defined as

$$y = \frac{1}{2}\ln\left(\frac{E + p_z}{E - p_z}\right). \tag{3.3}$$

These variables are convenient for the usage in the ATLAS experiment because $p_T, \phi$, and differences of $\eta$ are invariant under Lorentz-boost along the $z$-axis.

## 3.2.2. The Inner Detector
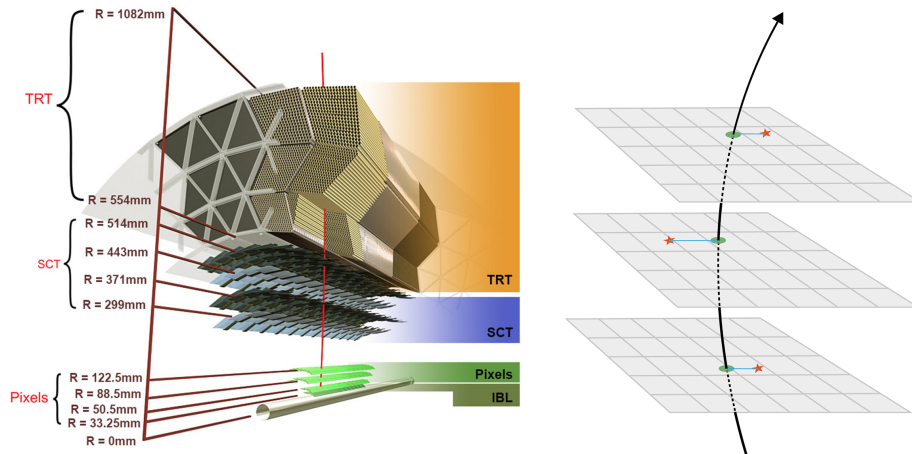


***Figure 3.1.:*** Schematic cross section of the inner detector of the ATLAS detector (© CERN).

The inner detector (ID) is the innermost part of the ATLAS detector. It is used for tracking charged particles, particle identification, and primary and secondary vertexing [54]. The ID consists of three different sub-detectors. Their rough structure is depicted in Figure 3.1. The ID is encapsulated with a solenoid magnet providing a 2 T axial magnetic field on the inside of the ID. The magnetic field is crucial to measure the momentum of a charged particle. The transverse momentum is measured as the curvature of the particle's track due to the Lorentz force.

The detector part closest to the beam pipe is the pixel detector. It consists of 1744

modules arranged in three barrel layers. Each module hosts 47232 silicon pixels with a size of $50 \times 400\,\mu\mathrm{m}^2$. The pixels are semiconductor trackers used to detect the traversing of charged particles.

The following part of the detector is the semiconductor tracker (SCT). It consists of 4088 modules arranged in four layers to guarantee four position measurements of charged particles. Each module consists of four silicon sensors. The sensors offer a $17\,\mu$m resolution in-plane lateral and $580\,\mu$m in-plane longitudinal.

The outermost part of the inner detector is the transition radiation tracker (TRT). It consists of polyimide drift (straw) tubes with a $4\,\mathrm{mm}$ diameter that are arranged in a $528\,\mathrm{mm}$ thick cylindrical layer around the beam pipe. The straw tubes are interleaved with fibres for the readout. The transition radiation tracker utilizes the transition light emitted by charged particles traversing the interface between two media with different indices of refraction. The TRT offers a measurement of charged particles and electron identification.

### 3.2.3. Calorimeter
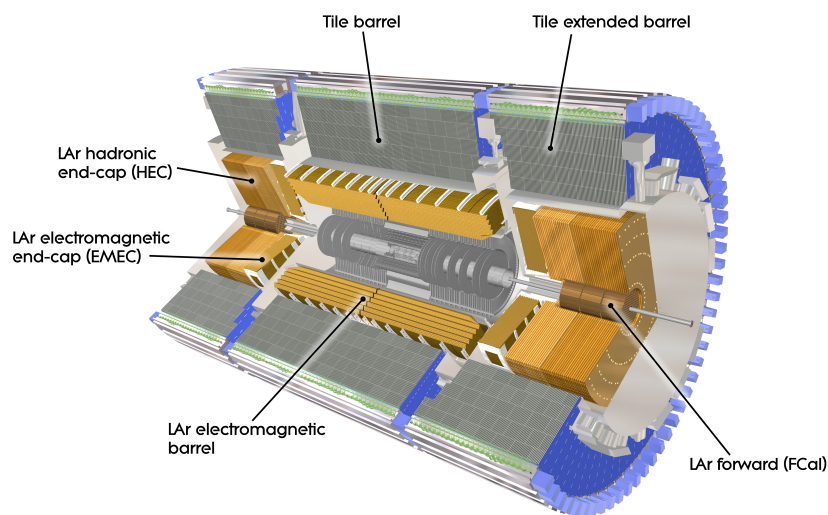


***Figure 3.2.:*** Computer generated image of the ATLAS calorimeter (© CERN).

The calorimeters are the detector layers following the inner detectors. Its structure is divided into the Electromagnetic calorimeter (ECal) and the hadronic calorimeter (HCal).

**Electromagnetic Calorimeter**

The ECal is used for the energy and position measurement of electric charged particles and photons. It utilizes bremsstrahlung and pair production to create a cascade of charged particles which are measured. It offers full azimuthal coverage and is equipped with end caps in the longitudinal direction of the beam pipe. The ATLAS ECal is a sampling calorimeter operating with lead as the passive and liquid Argon as the active medium. The innermost part of the ECal is a presampler which detects if the particle started showering before reaching the ECal.

**Hadronic Calorimeter**

The HCal measures the energy and position of baryons and mesons through strong interactions with the nuclei. In the range of $|\eta| < 1.7$ it is a sampling calorimeter with steel as the passive and scintillators as the active medium. For the end cap, liquid Argon is deployed as the active medium. The HCal works with the same principle as the ECal but offers less precise measurements.
In the range of $3.1 < |\eta| < 4.9$ ECal and HCal are substituted with the forward calorimeters (FCal) which are made up of three modules to fulfil the function of both calorimeters. In combination with the FCal a total range of $|\eta| < 4.9$ is covered by the calorimeters.
A computer-generated image of the structure of the different calorimeters used in the ATLAS detector is shown in Figure 3.2.

## 3.2.4. Muon Spectrometer

The muon spectrometer is the outermost part of the ATLAS detector. Its purpose is to detect charged particles exiting the calorimeters and measure their momentum in the range of $|\eta| < 2.7$. A detector dedicated to the measurement of muons is necessary because their mass makes them minimal ionizing particles in the energy range of the LHC collisions. The amount of energy loss due to bremsstrahlung is not sufficient to develop showers necessary to measure their energy. The muons' transverse momenta can be measured in the ID. Like the inner detector, the muon spectrometer utilizes a magnetic field to conduct a measurement of the particle's momentum. In the muon spectrometer, however, a solenoid magnet is used to allow for the measurement of the muon's momentum along a different direction. Combining the measurements, one obtains full knowledge of the muons four-momentum. Further, does the high rate of stopped electrons and hadrons in the calorimeters enable a high specificity in the muon detection.

### 3.2.5. Trigger System

With a bunch spacing of 25 ns [52] collisions happen at a rate of 40 MHz. Each collision involves up to hundreds of particles. To reduce the data to a feasible amount, triggers are employed to filter less interesting events. Different layers of triggers operate either at the hardware or software level. The L1 trigger is a hardware level trigger and acts as the first filter for the events. It makes decisions in less than $2.5\,\mu$s. The subsequent L2 trigger is a software level trigger and makes decisions in less than $200\,\mu$s. Combined the trigger system reduces the event rate from 40 MHz to 1000 Hz which are then stored at the CERN data centre.

# 4. Event Generation

## 4.1. Monte Carlo Event Generation
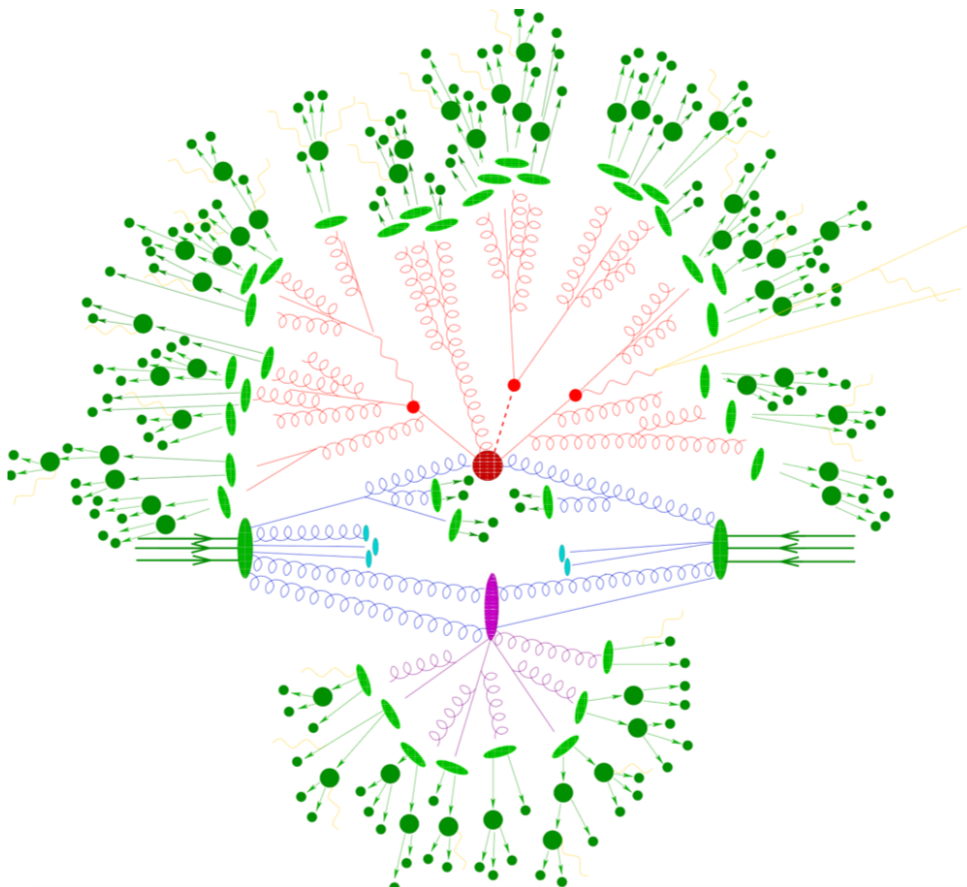


***Figure 4.1.:*** Schematic depiction of a decay cascade involving hadronic interaction at different energy scales [55].

The Monte Carlo event generation is the simulation of the physical process of a particle collision. The procedure for the calculation of these events usually consists of three different steps. These steps use different theories and approximations to deal with the different regions of the phase space and extreme values of $\alpha_S$. A schematic depiction of a decay cascade is shown in Figure 4.1.

**Matrix element generation** refers to the computation of the hard scattering of the partons. These calculations are usually done by considering a fixed order of the perturbation theory. This perturbative description is only applicable for $\alpha_S \ll 1$ which is the case for energies $Q > \mathcal{O}(100\,\text{GeV})$ [13]. The hard scattering is depicted as the red dot in the centre of Figure 4.1.

**Parton showers** refers to secondary QCD processes. They can occur from both the partons of the proton and the products of the underlying event. Parton showers describe the successive emission of other partons like gluons and quarks which are called showers. The resulting particles can be measured as jets in the detector. Various models are used to simulate the processes that lead to the formation of hadronic jets. This process takes place at energies of around $Q \sim \mathcal{O}(10\,\text{GeV})$. The Parton showers are shown as the red lines in Figure 4.1.

**Hadronization** refers to the process of creating bound states out of the partons. This process usually sets in as particles reach low energy scales of $Q \sim \mathcal{O}(1\,\text{GeV})$ where the coupling constant of QCD approaches $\alpha_S = 1$. Due to the value of $\alpha_S$, a perturbative description is not possible. Therefore, the simulation of this process is done using heuristic models like the Lund-String model or the cluster model [56–59]. This process is depicted as the green arrows and dots at the outermost part of Figure 4.1.

## 4.2. Detector Simulation

The ATLAS detector is limited in its detection capabilities. It is not able to directly identify the type of particles, but it can only measure the energy deposited by the particles. Further, there are uncertainties in the measurements due to its statistical nature and efficiencies in the detection of the particles. To compare the data with generated events, the latter are run through a detector simulation. A detector simulation uses the events generated by the Monte Carlo event generator and turns them into detector signals. This process has to take the inefficiencies, the uncertainties and the triggers of the detector into account. ATLAS uses GEANT for the simulation of its detector [60].

## 4.3. Signal and Background Simulation

Table 2.1 shows that most of the Higgs production originates from the ggF process. The Signal is modelled via $gg \to H^* \to ZZ$ at next to leading order. The main irreducible
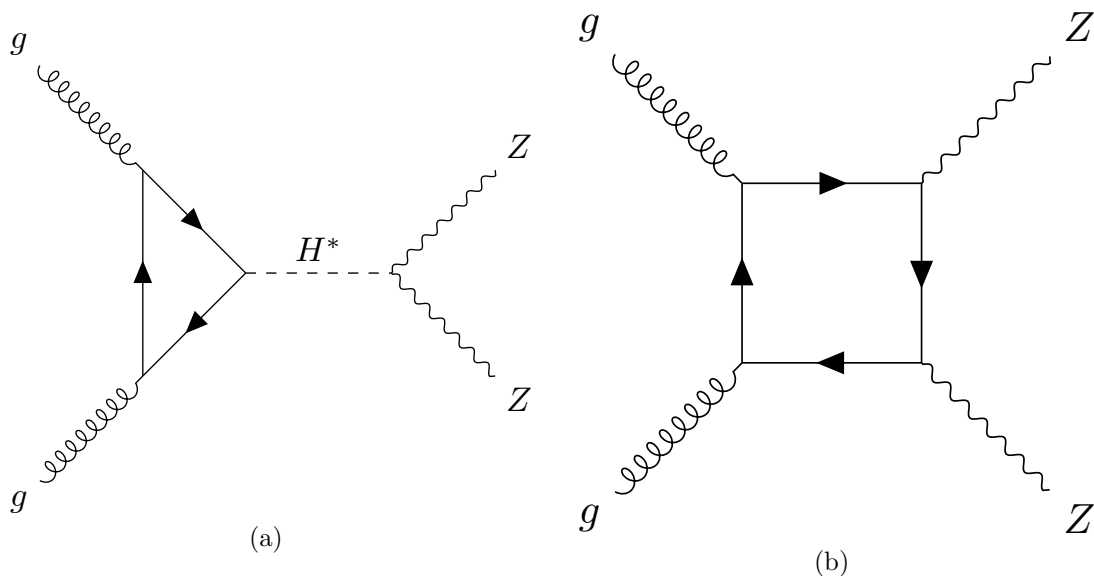
***Figure 4.2.:*** The leading-order Feynman diagrams for the $gg \to ZZ$ channel [61]. (a) is the $gg \to H^* \to ZZ$ signal process and (b) the $gg \to ZZ$ background process.

background comes from $gg \to ZZ$ and $qq \to ZZ$ production. The $gg \to ZZ$ process is modelled using MADGRAPH [62] and the $qq \to ZZ$ is simulated using SHERPA [63]. The MADGRAPH modelling of the $gg \to ZZ$ channel consists of an event generation of the $gg \to H^* \to ZZ$ process and an inclusive event generation of the $gg \to ZZ$ process. Since the inclusive modelling of the $gg \to ZZ$ process includes $gg \to H^* \to ZZ$ events, the modelling of the $gg \to ZZ$ background is done differentially as

$$\sigma(gg \to ZZ \text{ Background}) = \sigma(gg \to ZZ) - \sigma(gg \to H^* \to ZZ). \tag{4.1}$$

Such a treatment ensures that the interference between signal and background process is accounted for in the simulation. The two leading order Feynman diagrams for the signal and background process are depicted in 4.2. In the following, whenever referred to $gg \to ZZ$, the background process and its interference with the signal $gg \to H^* \to ZZ$ process is meant.

Due to current limitations in the model used to generate the $gg \to ZZ$ samples using MADGRAPH, only events in the $\mu^+\mu^-e^+e^-$ final state are modelled.

The simulation and analysis are performed at particle level, thus not taking detector or reconstruction inefficiencies into account. Therefore, the reduced cross section in the MADGRAPH samples can be adjusted by reweighting them with a factor of 2. Such a procedure does not corrupt the scaling of the samples because the branching ratio for the

| Channel | Cross section $\sigma(m(4\ell) > 180\,\text{GeV})$ in fb |
|---|---|
| $gg \to ZZ \to 4\ell$ (inclusive) | 3.31 |
| $gg \to H \to ZZ \to 4\ell$ | 0.0148 |
| $qq \to ZZ \to 4\ell$ (inclusive) | 53.3 |

***Table 4.1.:*** Cross section for the different processes calculated for a *pp*-collider at $\sqrt{s} = 13\,\text{GeV}$ at next-to-leading order. The calculations were performed using SHERPA for the $qq \to ZZ$ process and MADGRAPH for the $gg \to ZZ$ and $gg \to H \to ZZ$ process respectively. Note, that this includes the object definitions for the leptons as defined in Section 5.1.

for $ZZ \to 4e, 4\mu$ and $ZZ \to 2\mu2e$ are approximately identical, as seen in Table 2.3. Note that to prevent any imbalance due to the object definitions and acceptance ranges, the object definitions for $\mu$ and $e$ have to be identical.

## 4.3.1. Modelling of Polarised $H^* \to ZZ$ Samples

To model the contribution of the different polarisation states of the $ZZ$ system, specialised MADGRAPH samples containing only $Z_L Z_L$ and $Z_T Z_T$ events are generated [64]. The contribution of entangled polarisation states can not be modelled directly. Assuming the total cross section of the $ZZ$ system can be decomposed according to Eq. 2.40, the contribution of the entangled polarisation states is obtained via

$$\frac{d\sigma}{d\Omega_1 d\Omega_2}(Z_L Z_T) = \frac{d\sigma}{d\Omega_1 d\Omega_2}(ZZ) - \frac{d\sigma}{d\Omega_1 d\Omega_2}(Z_L Z_L) - \frac{d\sigma}{d\Omega_1 d\Omega_2}(Z_T Z_T)\,. \qquad (4.2)$$

On a more practical note, this means that there are no events with $Z_L Z_T$ to process, but the distribution is obtained by subtracting the histograms containing $Z_L Z_L$ respectively $Z_T Z_T$ events from the one generated from the inclusive $gg \to H^* \to ZZ$ process.

# 5. Event Selection

## 5.1. Object Definition

Lepton candidates are required to have a $p_T > 7\,\text{GeV}$. The limited coverage of the ATLAS detector also imposes constraints on the leptons' angular acceptance. Therefore, lepton candidates must satisfy $|\eta| < 2.47$. Since the influence of the crack region on this analysis was expected to be minuscule, it was not considered in the object definition. These acceptance ranges do not reflect the exact nature of the ATLAS detector, because its efficiency differs between electrons and muons. However, to ensure equivalent object definition of the leptons (as mentioned in Sec 4.3), of each criterium the stricter one was chosen.

Jets are defined using the anti-kt algorithm [65, 66] with radius parameter $R = 0.4$. They are required to have $|\eta| < 4.5$ and $p_T > 30\,\text{GeV}$. These cuts and requirements are implemented to take limitations of the detector coverage into account and to limit the number of considered leptons and jets not originating from hard scattering processes.

Since this analysis is done on particle level, no elaborate reconstruction is necessary. This would, however, become necessary when performing this analysis on actual data taken by the ATLAS Collaboration.

## 5.2. Preselection

The overall event selection strategy employed in this work follows the one of the ATLAS collaboration in the search for off-shell Higgs production [61].

The preselection requires that events contain two same flavour opposite sign (SFOS) lepton pairs, where $\ell = e, \mu$. Only events with $m(4\ell) > 180\,\text{GeV}$ are considered, which is the on-shell $ZZ$ production threshold. The $Z^0$ bosons' kinematics are reconstructed by combining the same-flavour opposite signed (SFOS) lepton pairs. In the $4e, 4\mu$ final states, where two pairings are possible, the first $Z^0$ boson is reconstructed as the pairing of leptons with the mass being closest to the actual $Z^0$ mass. The sub-leading $Z^0$ boson, $Z_2$, is obtained by combining the remaining two leptons. The reconstructed $Z^0$ boson candidates are

required to pass a $Z^0$ mass window cut which is defined as $m(\ell^+\ell^-) \in [70\,\mathrm{GeV}, 110\,\mathrm{GeV}]$. From here on, if not specified otherwise, all variables are taken in the laboratory system.

## 5.3. Event Selection

To suppress the different background contributions and obtain a pure signal and control region, a binary classification approach using a dense neural network (DNN) is used to separate signal and background events.

For this, a DNN is trained to distinguish between the $gg \to H^* \to ZZ$ and $qq \to ZZ$,$gg \to ZZ$ processes. Since the $qq \to ZZ$ background process has the highest cross section of the processes involved (see Table 4.1), suppressing its contribution in the signal region is the primary aim of this event selection. For the training of this DNN, the generated

| Variable | Description |
|---|---|
| $p_T(\ell_i)$ | transverse momentum of the $i$-th lepton |
| $\eta(\ell_i)$ | pseudorapidity of the $i$-th lepton |
| $E(\ell_i)$ | energy of the $i$-th lepton |
| $m(Z_i)$ | invariant mass of the $i$-th $Z^0$ boson |
| $\eta(Z_i)$ | pseudorapidity of the $i$-th $Z^0$ boson |
| $N_{jets}$ | number of jets |
| $\not{E}_\mathrm{T}$ | missing transverse energy |
| $\Delta R(ZZ)$ | angular difference of the $Z^0$ bosons: $\sqrt{(\Delta\eta)^2 + (\Delta\phi)^2}$ |

***Table 5.1.:*** Input variables of the $O_{NN}^{HZZ}$ DNN.

| Variable | Description |
|---|---|
| $p_T(\ell_i)$ | transverse momentum of the $i$-th lepton |
| $\eta(\ell_i)$ | pseudorapidity of the $i$-th lepton |
| $\phi(\ell_i)$ | polar angle of the $i$-th lepton |
| $E(\ell_i)$ | energy of the $i$-th lepton |
| $E(Z_i)$ | energy of the $i$-th $Z^0$ boson |
| CoM $Z_i$ $\eta(\ell^+)$ | pseudorapidity of the positive lepton emitted by $Z_i$ in its centre of mass frame |
| $Z_i$ $\Delta\phi(\ell^+\ell^-)$ | angle between the two leptons emitted by $Z_i$ in the four-lepton centre of mass frame |

***Table 5.2.:*** Input variables of the $O_{NN}^{TT}$ DNN.

samples of the $qq \to ZZ$ are used as background and $gg \to H^* \to ZZ$ as the signal. Note here, that the $gg \to ZZ$ is not used for the training of the DNN. The modelling of the

| Region | Requirement | Variable |
|--------|-------------|----------|
| SR | $O_{NN}^{HZZ} > 0.2$ | $O_{NN}^{TT}$ |
| CR | $O_{NN}^{HZZ} \leq 0.2$ <br> $m(4\ell) \in [180\,\mathrm{GeV}, 400\,\mathrm{GeV}]$ | $m(4\ell)$ |

***Table 5.3.:*** Definition of Signal and Control Regions.

$gg \to ZZ$ process is done inclusively. Thus, the sample contains events originating from $gg \to ZZ$ background processes as well as those from the $gg \to H \to ZZ$ signal process. So training the DNN to treat these events as background limits its ability to separate the $gg \to H^* \to ZZ$ events, because the inclusive $gg \to ZZ$ samples contains as much $gg \to H^* \to ZZ$ events as the sample containing exclusively $gg \to H^* \to ZZ$ events. The most promising way would be, to simulate a $gg \to ZZ$ sample not containing the $gg \to H^* \to ZZ$ process and use it in the training. This was however not done, because such a sample was not accessible, at the time of this work. The input variables utilised by the DNN are given in Table 5.1. The layout for this DNN is chosen as four layers each with 30 nodes.

Another DNN is trained to separate between events of the form $gg \to H^* \to Z_L Z_L$ and $gg \to H^* \to Z_T Z_T$. This is done to obtain a variable, that is sensitive to the polarisation state of the $ZZ$ system. Since events originating from $gg \to H^* \to Z_L Z_T$ processes are not directly accessible, as elaborated in Chapter 4.3.1. Thus, the DNN can not be trained to be sensitive to both $gg \to H^* \to Z_L Z_T$ and $gg \to H^* \to Z_T Z_T$. Instead, it is trained to separate among the $gg \to H^* \to Z_L Z_L$ and $gg \to H^* \to Z_T Z_T$ events, which are accessible via the MADGRAPH modelling mentioned in Chapter 4.3.1. The input variables used for this DNN are given in Table 5.2. The layout of the DNN was chosen as five layers with 30 nodes each. The more complex structure was used because the MADGRAPH samples contained more events and thus limiting the effects of overtraining. The training and validation of the DNN are done via a k-fold with two folds. A hyper-parameter optimization was not performed for either of the DNNs because a more thorough analysis of the deployment possibilities of deep learning is beyond the scope of this work. The distribution of the input variables can be found in the appendix.

These event selection flags are used to define a Signal Region (SR) and a Control Region (CR). The regions are defined in Table 5.3. The definition of these regions is chosen to reduce the dominant $qq \to ZZ$ and $gg \to ZZ$ background in the signal region and ensure a precise normalisation of the background contribution. The very loose criterium of $O_{NN}^{HZZ} > 0.2$ is chosen to prevent a significant reduction of the $Z_T Z_T$ and $Z_L Z_T$ contribu-

tions (More to be found in Chapter 6.1).

The small cross section makes it impractical to define multiple signal regions or control regions because each of them would have small yields and therefore large statistical uncertainties. Aside from that, it comes with practical complications because the $Z_T Z_L$ component is modelled as the difference of $ZZ$ and $Z_L Z_L$, $Z_T Z_T$ (see Chapter 4.3.1), which can lead to negative entries in some bins causing problems during the fitting procedure.

# 6. Study of the Entanglement Testing Properties

## 6.1. Assessment of the Event Selection



(a)                                                    (b)
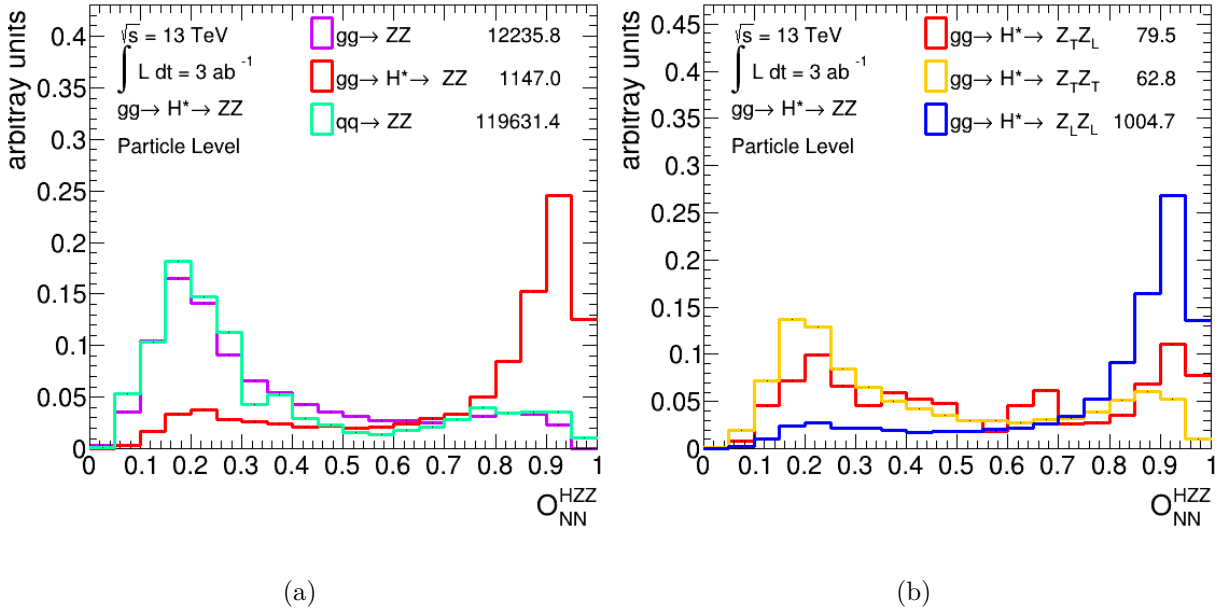
***Figure 6.1.:*** The output variable of the event selection DNN $O_{NN}^{HZZ}$ for the signal and background contribution in (a) and the different polarisation states of $gg \rightarrow H^* \rightarrow ZZ$ in (b). Each distribution is normalised to unity.

The output of the event selection DNN $O_{NN}^{HZZ}$ is shown in Figure 6.1. The shape of the distribution belonging to the $qq \rightarrow ZZ$ and $gg \rightarrow ZZ$ processes in Figure 6.1(a), indicates that for high values of $O_{NN}^{HZZ}$ the signal purity is high. It is notable, that this variable suppresses both the $qq \rightarrow ZZ$ and $gg \rightarrow ZZ$ background, even though, it was not trained to suppress the $gg \rightarrow ZZ$ background. In Table 6.1 the signal-to-background ratio is shown for different cuts on $O_{NN}^{HZZ}$. A cut at 0.9 would give a signal-to-background ratio of 13.8%. So this variable can suppress the background and give a pure signal region.

| Sample | $O_{NN}^{HZZ} > 0.8$ | $O_{NN}^{HZZ} > 0.9$ | Total |
|:---:|---:|---:|---:|
| $gg \to ZZ$ | 698.5 | 62.5 | 12509.2 |
| $qq \to ZZ$ | 9259.9 | 2472.7 | 142049.5 |
| $gg \to H^* \to ZZ$ | 671.0 | 349.7 | 1183.5 |
| SG/BG-Ratio | 0.067 | 0.138 | 0.0077 |

***Table 6.1.:*** Yields and signal-to-background-ratio for different cuts on $O_{NN}^{HZZ}$.

In Figure 6.1(b) the distributions of the polarisation states of the $ZZ$ system for the $O_{NN}^{HZZ}$ are depicted. One can see that the shape of these distributions differs. The $O_{NN}^{HZZ}$-distribution of $gg \to H^* \to Z_T Z_T$ events resembles the distributions of the background processes. This distribution peaks at low values of $O_{NN}^{HZZ}$ but has a broad tail with near-constant behaviour for values of $O_{NN}^{HZZ} > 0.4$. For the $gg \to H^* \to Z_L Z_T$ events, the distribution has less significant peaks but comes with a double-peaked structure with peaks at low and high values of $O_{NN}^{HZZ}$ and near constant behaviour in between.

The receiver operator characteristics (ROC) curve of a binary classifier is a graph depicting its separation qualities. It displays the false positive rate as abscissa and the true positive rate as ordinate for varied thresholds of the classifier as a discriminator.

A quantity derived from the ROC curve is the area-under-curve (AUC). It is the area under the ROC curve of a classifier and takes values between 0.5 and 1. The AUC is a direct measure of the separation qualities of a binary classifier, with higher values corresponding to a better separation. An AUC of 1 would correspond to a perfect classifier, whereas a value of 0.5 would correspond to a random classifier.

The permutation importance provides a measure of the influence a variable has on the output of the classifier. It is given by

$$\frac{\text{AUC}_{\text{nom}} - \text{AUC}}{\text{AUC}_{\text{nom}}} \tag{6.1}$$

where $\text{AUC}_{\text{nom}}$ is the AUC of the classifier itself and AUC is the AUC of the classifier, but with the input of the examined variable substituted with random noise. Higher values correspond to a larger influence of the variable on the classifier.

Figure 6.2 shows evaluation plots for the DNN of $O_{NN}^{HZZ}$. From the permutation importance of the input variables depicted in Figure 6.2, it can be concluded that the $p_T$ values of the leptons have the biggest impact on the DNNs output. Considering that the invariant mass of the four lepton system was not provided as an input variable, this appears only natural because the $p_T$ is highly correlated with $m(4\ell)$. The invariant mass of the $m(4\ell)$ however is one of the most important variables in terms of separation of

(a)

(b)

(c) Fold 0

(d) Fold 1
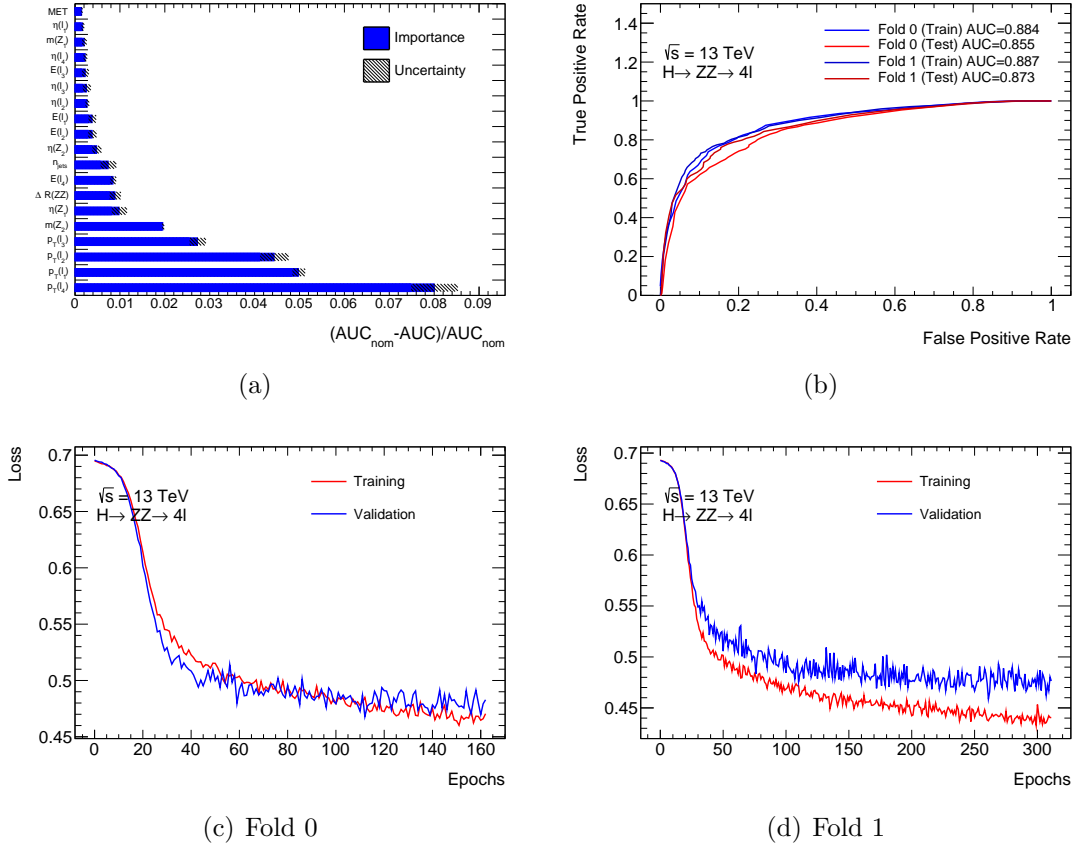
***Figure 6.2.:*** Evaluation plots for the DNN of $O_{NN}^{HZZ}$. Figure (a) shows the permutation importance of the input variables, which is a measure of the contribution of this variable to the output calculated by the DNN. Figure (b) shows the ROC curves for validation and training for the two folds. Figure (c) and (d) show the loss value over the course of the training of the DNN for the two folds.

$gg \rightarrow H^* \rightarrow ZZ$ from [61]. This behaviour of the system is also evident from Figure 6.7, showing the distribution of the invariant mass for the different channels. For high values of $m(4\ell)$ the contribution of the $gg \rightarrow H \rightarrow ZZ$ signal events dominates. The ROC curve depicted in Figure 6.2(b) shows small differences between the two folds for each of the training curves. The validation curve for one of the two folds does not only differ significantly from the training curve of the same fold but also from the curves belonging to the other fold. This indicates that the training of this DNN is limited by the number of events in the sample. Since the two folds show some statistical fluctuations. The smaller AUC for training than for the validation sample, indicates effects of overtraining in the training process of the DNN. Overtraining is also featured in the loss curves of the DNN training process depicted in Figure 6.2(c) and 6.2(d). Here the effect is again more

35

significant in one of the two folds. The shape of the ROC curve and the AUC of around
0.86 show the limited separation qualities of this classifier. Note, that the calculations
of all these evaluation plots are done only considering the samples that were used in the
training procedure. For this DNN these are the two samples containing $gg \to H \to ZZ$
and $qq \to ZZ$ events.



(a)                                                                (b)
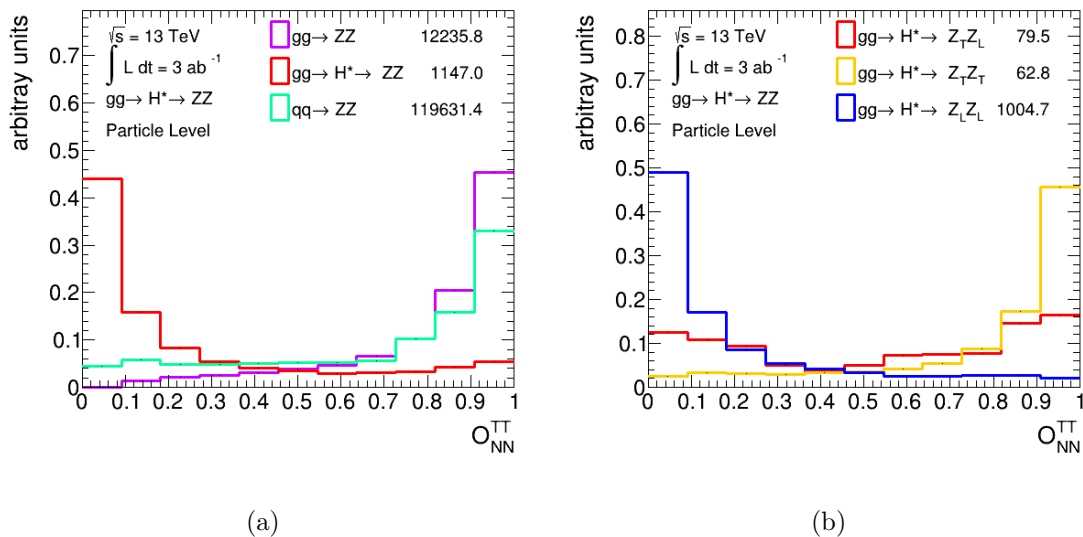
**Figure 6.3.:** The output variable of the event selection DNN $O_{NN}^{TT}$ for the signal and
background contribution in (a) and the different polarisation states of $gg \to$
$H^* \to ZZ$ in (b). Each distribution is normalised to unity.

The classifier for the polarisation states has a high sensitivity for longitudinally and trans-
verse polarised events. These events are well separated, as seen in Figure 6.3(b): The
number of $Z_L Z_L$ events peaks at low values of $O_{NN}^{TT}$ and the number of $Z_T Z_T$ events
peaks at high values of $O_{NN}^{TT}$. The sensitivity for the entangled contributions on the other
hand is low. These events show a double-peaking structure at values close to 0 or 1. This
is linked to the training of the DNN. Because the DNN was not trained to separate the
$Z_T Z_T$ and $Z_T Z_L$ component from $Z_L Z_L$ but only $Z_T Z_T$ and $Z_L Z_L$, due to the inaccessibil-
ity of $Z_L Z_L$ events. However, as seen in Figure 6.4(a), when only taking $gg \to H^* \to ZZ$
events into account, the $O_{NN}^{TT}$ is very sensitive for transverse and entangled events since
they make up most of the yields at high values of $O_{NN}^{TT}$.
From the shape of the signal and background distributions for $O_{NN}^{HZZ}$ which is depicted in
6.3(a), it can be seen that the two background channels peak at 1 while the signal events
peak at 0. The latter is expected, because the $gg \to H^* \to ZZ$ is mostly made up of
longitudinally polarised events, which the DNN is trained to suppress.
The evaluation plots for this DNN are shown in 6.5. From the permutation importance

(a) Preselection Cuts
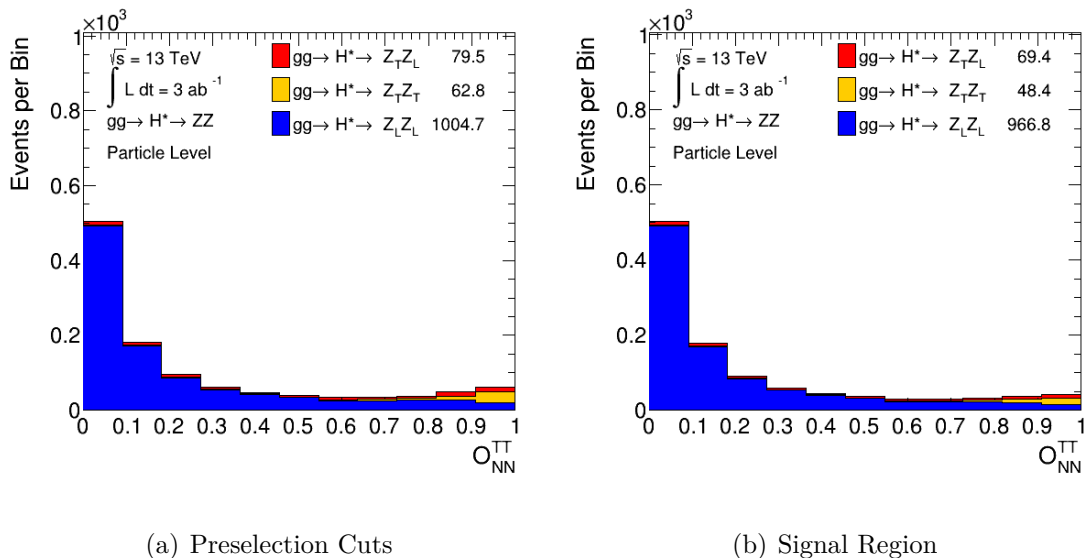
(b) Signal Region

***Figure 6.4.:*** The distribution of $O_{NN}^{TT}$ for the $gg \rightarrow H^* \rightarrow ZZ$ process (a) with only preselection cuts and (b) in the signal region.

depicted in 6.5(a), the separation angles $\Delta\phi(\ell^+\ell^-)$ between the two leptons emitted by one of the $Z^0$ bosons in the centre of mass of the four leptons is identified as the most important variable. Within the centre-of-mass frame of each of the $Z^0$ bosons, the two leptons are back-to-back. The angle in the four leptons reference frame, however, is distorted by the Lorentz boost between the two systems. The effect of this is dependent on the $\gamma$-factor of the Lorentz boost and the direction of the two leptons relative to the $Z^0$ movement axis. The $\gamma$ factor of this transformation is given by

$$\gamma = \frac{E(Z_i)}{m(Z_i)} \tag{6.2}$$

Since the $Z^0$ mass is fixed, $\gamma$ is linearly dependent on the energy $Z^0$. The energy of the $Z^0$ within the four leptons rest frame on the other hand is directly related to the $m(4\ell)$, because the two $Z^0$ are back-to-back their energy is given by

$$E(Z) = \frac{m(4\ell)}{2} \, . \tag{6.3}$$

Therefore, the $\gamma$-factor itself is linearly dependent on the invariant mass of the four lepton system.

The angle $\theta$ between the leptons and the $Z^0$ axis of movement also influences the angle between the lepton in the four lepton rest frame. Larger values of $\theta$ lead to smaller values for $\Delta\phi(\ell^+\ell^-)$. From Equation 2.31 and 2.34 it is known, that the longitudinally polarised

(a)



(b)



(c) Fold 0



(d) Fold 1
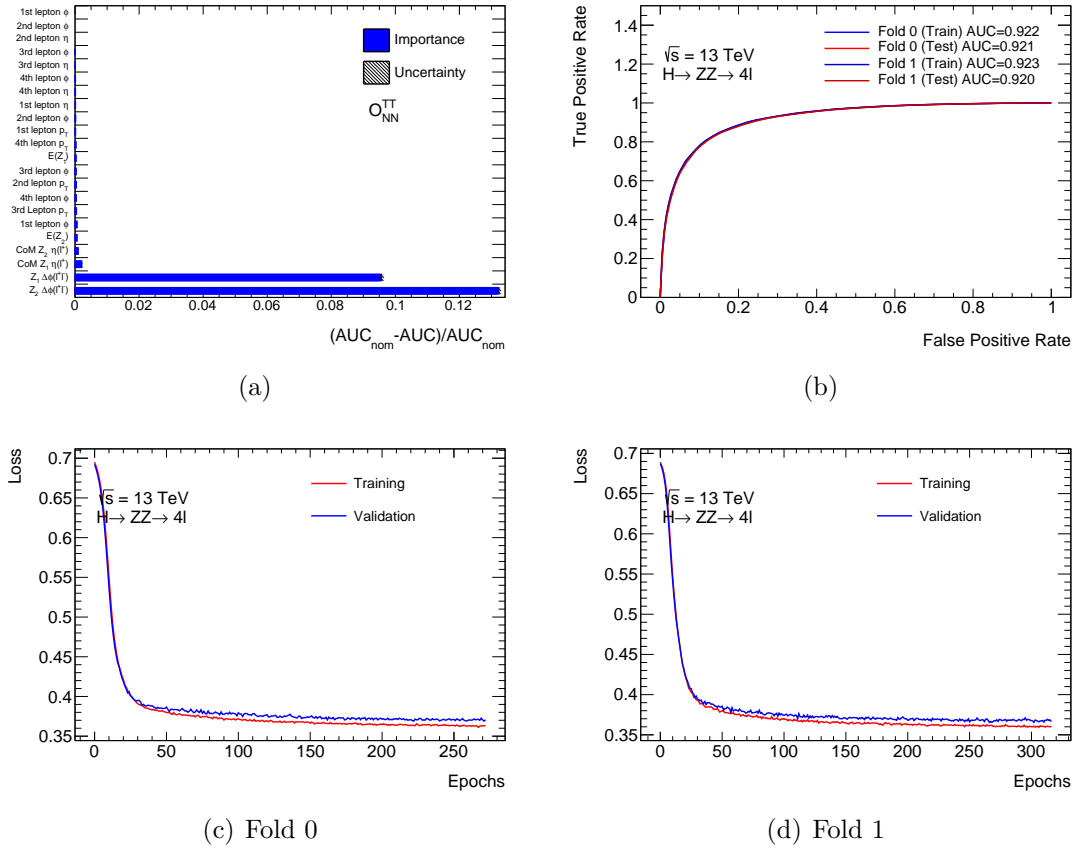
***Figure 6.5.:*** Evaluation plots for the DNN of $O_{NN}^{TT}$. Figure (a) shows the permutation importance of the input variables, which is a measure of the contribution of the variable on the output calculated by the DNN. Figure (b) shows the ROC curves for validation and training for the two folds. Figure 6.5(c) and 6.5(d) show the loss value over the course of the training of the DNN for the two folds.

$Z^0$ boson decay preferably perpendicular to the axis of movement of the $Z^0$ whereas the transverse polarised $Z^0$ bosons decay preferably collinear with the axis of movement. This circumstance can also be seen in Figure A.10. The distribution of $\cos(\theta)$ shows the behaviour theoretically predicted in Chapter 2.2.2 for the case longitudinally and transverse polarised $Z^0$ boson pairs.

Thus, this angular variable is potent in separating the polarisation states because it combines two distinct features of these; the dependence on the four-lepton invariant mass and the emittance angle of the leptons relative to the $Z^0$ bosons momentum. The distribution of this variable can be found in Figure B.10(e) and B.10(f).

The ROC curve in Figure 6.5(b) for the different folds show no visible difference and the AUC coincides up to the third decimal. The loss curves in Figure 6.5(c) and 6.5(d) show

little difference between the training and validation sample, indicating that the effects of overtraining are quite low for this DNN. This behaviour can be explained by the larger number of events in the MADGRAPH samples. The AUC of 0.92 is high, showing that the classifier performs well at separating the two processes. Note, that the calculations of all these evaluation plots are done only considering the samples that were used in the training procedure, which for this DNN are, the two samples containing $gg \to H \to Z_L Z_L$ and $gg \to H \to Z_T Z_T$ events.
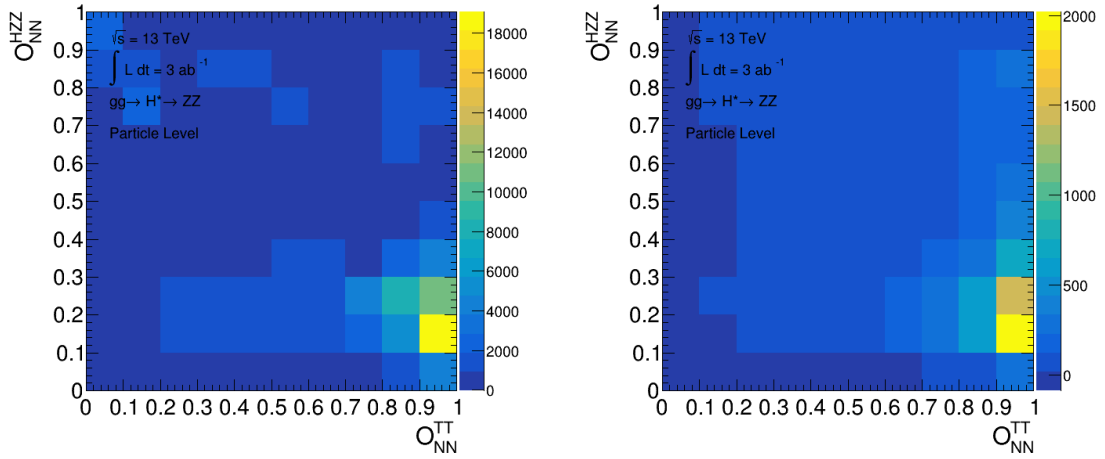
(a) $qq \to ZZ$

(b) $gg \to ZZ$
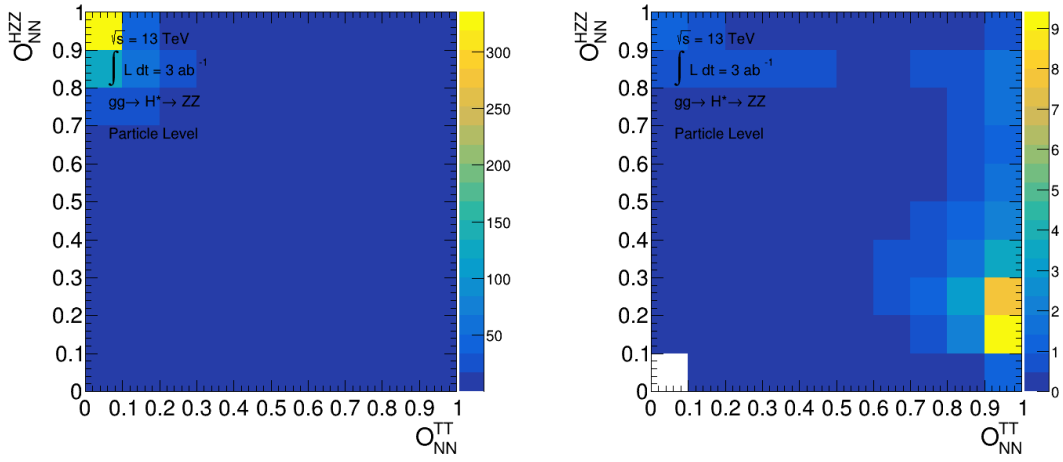
(c) $gg \to H^* \to Z_L Z_L$

(d) $gg \to H^* \to Z_T Z_T$
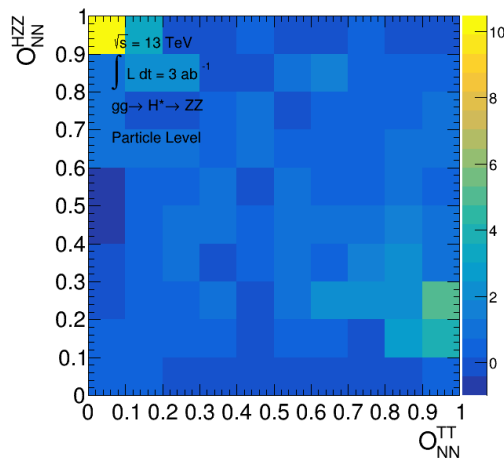
(e) $gg \to H^* \to Z_L Z_T$

***Figure 6.6.:*** Plots showing the distribution of the two DNN output variables for the different decay channels and background processes.

In Figure 6.6 the two classifiers are plotted. These graphs show a concentration of events at either $O_{NN}^{HZZ} = 0$ and $O_{NN}^{TT} = 1$ or $O_{NN}^{HZZ} = 1$ and $O_{NN}^{TT} = 0$. This indicates a negative



**(a)**                    **(b)**
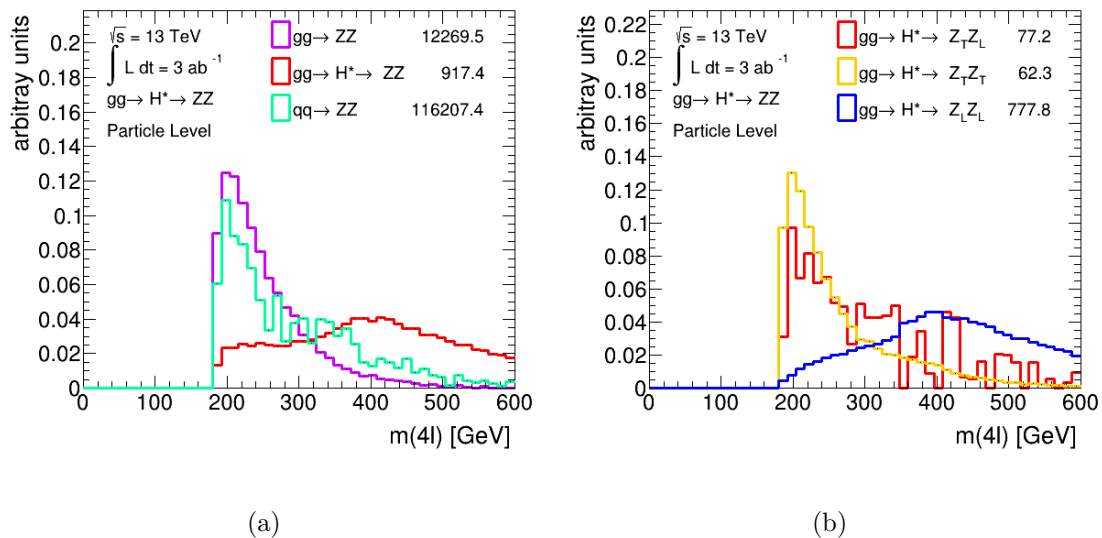
***Figure 6.7.:*** Distribution of the invariant mass of the four lepton system. Each distribution is normalised to unity. (a) shows the distribution of the background processes $gg \rightarrow ZZ$, $qq \rightarrow ZZ$, and the signal process $gg \rightarrow H \rightarrow ZZ$ respectively. (b) shows the distribution of the different polarisation states of the signal process.

correlation between the two classifiers. Such a behaviour heavily limits the possibility to define signal regions, with a high number of $gg \rightarrow H^* \rightarrow ZZ$ without losing the sensitivity to the contribution of $Z_T Z_T$ and $Z_T Z_L$. From Chapter 2.2.1 it is known, that events with higher invariant mass $m(4\ell)$ tend to be more longitudinally polarised. The invariant mass is also an important variable to separate the $gg \rightarrow H^* \rightarrow ZZ$ process from its background [61]. From Figure 6.7 it can be seen, that the $gg \rightarrow H^* \rightarrow ZZ$ contribution becomes largest for high values of $m(4\ell)$. As a consequence, cuts on $O_{NN}^{HZZ}$ lead to a reduction of the $Z_T Z_T$ component. Such a behaviour is problematic, because even though the $O_{NN}^{HZZ}$ allows for the definition of a signal region with a high signal-to-background ratio as presented in Table 6.1 which however would have no significance for transverse polarised $Z^0$ boson decays.

From the event yields depicted in Table 6.2 one can calculate the ratio of $gg \rightarrow H^* \rightarrow ZZ$ and background events in the signal region. For the different regions this ratio amounts

| Sample | SR | CR |
|--------|-----|-----|
| $Z_L Z_L$ | $1010 \pm 80$ | $22.5 \pm 1.9$ |
| $Z_T Z_T$ | $49.3 \pm 2.1$ | $14.4 \pm 1.0$ |
| $Z_L Z_T$ | $74.5 \pm 3.1$ | $13.1 \pm 0.6$ |
| $gg \to ZZ$ | $8700 \pm 400$ | $3550 \pm 250$ |
| $qq \to ZZ$ | $85200 \pm 3300$ | $46500 \pm 3100$ |
| Total | $95000 \pm 4000$ | $50100 \pm 3300$ |

***Table 6.2.:*** Yields of the different processes in the fit regions (for their definition see Chapter 5.3). Note that the uncertainties given here, are purely statistical uncertainties, as systematic uncertainties are not included in this analysis.

to

$$R_{SR} = \frac{N(gg \to H^* \to ZZ)}{N(\text{Background})} = 0.0121 \pm 0.0009 \tag{6.4}$$

$$R_{CR} = \qquad\qquad = 0.00099 \pm 0.00005 \,. \tag{6.5}$$

The acceptance of the event selection differs substantially for the different polarisation states. They are given by

$$\epsilon_{LL} = \frac{N(Z_L Z_L, SR)}{N(Z_L Z_L)} = 0.97 \pm 0.09 \,, \tag{6.6}$$

$$\epsilon_{TT} = \frac{N(Z_T Z_T, SR)}{N(Z_T Z_T)} = 0.77 \pm 0.04 \,, \tag{6.7}$$

$$\epsilon_{LT} = \frac{N(Z_L Z_T, SR)}{N(Z_L Z_T)} = 0.85 \pm 0.05 \,. \tag{6.8}$$

Here $N(x, SR)$ refers to the number of events of sample $x$ within SR. From this, one can see that the number of entangled and transverse polarised events is decreased substantially more than the number of longitudinally polarised events. This leads to a loss of significance for the test of entanglement in the signal region. This effect can also be seen in Figure 6.4 where the distribution of $O_{NN}^{TT}$ is shown with preselection cuts only and in the signal region. From there, it can be seen that a lot of the sensitivity for the contribution of transverse polarisation states is lost in the signal region. Note, that this effect increases with a more restrictive cut on $O_{NN}^{HZZ}$ as it can be seen from the shape in Figure 6.1(b). The reasons for this behaviour were elaborated in the analysis of the two DNN outputs. The distributions of the various kinematic variables depicted in the Appendix B show a strongly fluctuating behaviour for the $gg \to H^* \to Z_L Z_T$ process. This circumstance is a consequence of the way this process was modelled. The number of events per bin

is calculated as the difference of the full $gg \to H \to ZZ$ process and the number of events originating from longitudinal respectively transverse polarised $ZZ$ states. Thus, the uncertainties for the $gg \to H^* \to Z_L Z_T$ process are enhanced, which also results in the fluctuation observable in the plots.

## 6.2. Fitting Setup

To test for entanglement, a binned profile likelihood fit is performed. The distribution in the $ZZ$ channel can be decomposed into contributions coming from $gg \to ZZ$ and $qq \to ZZ$. The $gg \to ZZ$ can now be further separated into different parts, giving

$$\sigma(ZZ) = \sigma(qq \to ZZ) + \sigma(gg \to ZZ) + \sigma(gg \to H^* \to ZZ) + \sigma(\text{Interference}) \,. \quad (6.9)$$

The term $\sigma(\text{Interference})$ describes the interference of the $gg \to ZZ$ process without the Higgs propagator and the $gg \to H^* \to ZZ$ process. As this work aims to examine the quantum entanglement of the $ZZ$ system, the $gg \to H^* \to ZZ$ part is split up into the different polarisation states, giving

$$\sigma(ZZ) = \sigma(gg \to H^* \to Z_L Z_L) + \sigma(gg \to H^* \to Z_T Z_T) + \sigma(gg \to H^* \to Z_L Z_T)$$
$$+ \sigma(qq \to ZZ) + \sigma(gg \to ZZ) + \sigma(\text{Interference}) \,.$$
$$(6.10)$$

To get an estimate of the significance at which entanglement can be probed, an Asimov fit is performed. This refers to a fit where the stacked histograms of signal and background are used for the distribution to be fitted against. A detailed analysis of the systematic uncertainties of this process would be out of the scope of this work. Due to the small cross section of the Higgs off-shell process in general and the $H^* \to ZZ$ process in particular, the statistical uncertainties in this process are expected to dominate. Therefore, only statistical uncertainties are considered in this fit. The Asimov fit is performed because an application of this formalism to data would require a more thorough treatment of the involved background and optimisation of the DNNs and systematic uncertainties. This includes taking into account the various effects of the detector such as miss identification and uncertainties of the measurement.

For matters of convenience, the different background contributions are grouped. Therefore, the distribution used to fit is

$$\sigma(ZZ) = \mu_{LL} \cdot \sigma(Z_L Z_L) + \mu_{QE} \cdot (\sigma(Z_T Z_T) + \sigma(Z_L Z_T)) + \mu_{BG} \cdot \sigma(\text{Background}) \,. \quad (6.11)$$

The fit is performed using the distribution of the variables named in Table 5.3. For the signal region, the distribution of $O_{NN}^{TT}$ was used, because it is sensitive to the polarisation state of the $ZZ$ system. Therefore, it allows to test the contribution of the different polarisations states. The invariant mass in the control region was chosen because it is expected to have small fluctuations allowing for a precise normalisation of the background. Due to the complex event selection employed, a fit directly to a theoretically obtained distribution is not possible. Instead, the different histograms are multiplied with norm factors which are adjusted during the fitting procedure. Since the different distributions are not fitted to data but to the sum of the distributions themselves, the optimal value for each norm factor is 1 by construction. The uncertainty of the values can be used to estimate the significance of the test for entanglement. The pre-fit plots depicting the signal and control regions are given in the appendix.

## 6.3. Fit Results

**Table 6.3.:** Fitted values for the norm factors for $\mathcal{L} = 3\,\mathrm{ab}^{-1}$ for different values of background scaling.

| Background scaling | $\mu_{QE}$ | $\mu_{LL}$ | $\mu_{BG}$ |
|:---:|:---:|:---:|:---:|
| 1 | $1.00 \pm 6.16$ | $1.00 \pm 2.11$ | $1.00 \pm 0.07$ |
| 0.75 | $1.00 \pm 5.62$ | $1.00 \pm 0.91$ | $1.00 \pm 0.03$ |
| 0.5 | $1.00 \pm 6.41$ | $1.00 \pm 1.24$ | $1.00 \pm 0.14$ |
| 0.25 | $1.00 \pm 7.83$ | $1.00 \pm 0.80$ | $1.00 \pm 0.14$ |
| 0.10 | $1.00 \pm 7.99$ | $1.00 \pm 0.25$ | $1.00 \pm 0.10$ |
| 0.05 | $1.00 \pm 7.37$ | $1.00 \pm 0.14$ | $1.00 \pm 0.10$ |
| 0.01 | $1.00 \pm 1.29$ | $1.00 \pm 0.05$ | $1.00 \pm 0.13$ |
| 0 | $1.00 \pm 0.19$ | $1.00 \pm 0.04$ | - |

First, the full distribution as described above was fitted, to get an estimate of the expected significance. The fit was performed in the two regions described in Chapter 5.3. In the appendix, Figures showing the plots corresponding to theses regions are shown. The results of the norm factors are given in Table 6.3. The norm factors lie indeed as constructed at 1. From the uncertainty of $\mu_{BG}$ one can extract the significance. For the background rejection efficiency of this work, which corresponds to a background scaling of 1, the significance amounts to

$$0.16\,\sigma_{QE}\,. \tag{6.12}$$

To get an estimate of what background rejection efficiency is necessary to test entanglement at a certain sensitivity the same fit is performed for different values of scaling of the background. Notable is, that the significance does not increase monotonously with a decreased background scaling. The behaviour is most likely to result from the way the background was modelled and the correlation between the norm factors $\mu_{BG}$ and $\mu_{QE}$. The correlation matrices for the norm factor are depicted in the appendix in Figure A.11. With smaller background scaling the norm factor $\mu_{BG}$ and $\mu_{QE}$ become more correlated. From the shape of the distributions of $O_{NN}^{TT}$ in Figure 6.3, it can be seen that the distribution of the background resembles that of the $gg \to H^* \to Z_T Z_T$. Thus if the scaling of the background becomes smaller and its yield approach that of the $gg \to H^* \to Z_T Z_T$ and $gg \to H^* \to Z_L Z_T$, the norm factors become more correlated [1]. However, it is limiting the ability to estimate the required background rejection efficiency.

For a background scaling of 0, which corresponds to an absolutely pure signal region, the significance is

$$5.26\,\sigma_{QE}\,. \tag{6.13}$$

Note that this already takes the decreased acceptance for the $Z_L Z_T$ and $Z_T Z_T$ states into account.

A fit not taking any further event selection along the preselection into account is performed as well. This corresponds to a fit of the $gg \to H^* \to ZZ$ events with the distribution of $O_{NN}^{TT}$. For this case the significance amounts to

$$7\,\sigma_{QE}\,. \tag{6.14}$$

Due to the nature of this fit and the resulting norm factor with concurring values of 1, the pre- and post-fit plots are identical. They can be found in the appendix.

---

[1] A full investigation of the effects leading to this unusual behaviour is postponed because it would exceed the time frame of this work.

# 7. Conclusion and Outlook

This thesis investigated the sensitivity of entanglement in $H^* \to ZZ \to 4\ell$ events.

The condition for entanglement is turned into a binary test between a solely longitudinally polarised $ZZ$ system and an entangled $ZZ$ system containing contributions from longitudinally, transverse polarised and entangled $ZZ$ boson polarisation states. For this analysis, solely longitudinally and transverse polarised $H^* \to ZZ$ events were simulated. The distributions of these events were then compared with those originating from the inclusive $gg \to H^* \to ZZ$ process. This approach allowed to model the contributions from the different polarisation states independently.

A dense neural network was employed for the background rejection, to define signal regions with an enhanced number of $gg \to H^* \to ZZ$ events. To obtain a variable sensitive to the polarisation of the $ZZ$ boson state, another dense neural network was trained to separate among events from longitudinally and transverse polarised $Z^0$ bosons. Using this variable, a profile likelihood fit was performed on an Asimov dataset, to examine the sensitivity for entanglement in this analysis.

The expected significance which can be probed with the current setup is $0.16\,\sigma$. Therefore, it is not expected to be measurable in experimental data. Because for experimental data the significance is further impaired by reconstruction inefficiencies and limitations in the detector resolution.

This low sensitivity appears mostly due to the large background contamination in the signal region. The background classifier employed in this analysis has a high sensitivity for $gg \to H^* \to ZZ$ events. In principle, this would allow to define signal regions with a high signal-to-background ratio. However, the distributions of the classifier $O_{NN}^{HZZ}$ are different for the polarisation states of the $ZZ$. Thus, cuts on this classifier diminish the number of $Z_L Z_T$ and $Z_T Z_T$ events. To not lose the sensitivity for these different polarisation states in the signal region, the cut on the background rejection classifier is chosen very loose, leading to large background contamination.

Without the consideration of the background events, the sensitivity achieved was $5.3\,\sigma$. When not taking the decreased acceptance into account, the sensitivity increases to $7\,\sigma$. This, of course, poses an unrealistic scenario but indicates that probing entanglement

becomes possible with a sufficient background rejection. The fluctuation of the significance for different background rejection makes it impractical to assess the efficiency of background rejection necessary to probe entanglement.

One way this analysis may be improved would be with a more concise modelling of the background. The background modelling might be differentiated into the processes contributing. This would allow to account the norm factors for the interference between processes sharing initial and final states with the signal process.

The event selection can be improved in several manners. One possibility would be to employ a pseudo matrix element formalism, as it was done by the ATLAS Collaboration in the search for off-shell Higgs production [61]. Whether such a formalism is suited, is difficult to assess, because it has to address two problems at the same time. It has to deliver a sufficient background rejection efficiency, without diminishing the sensitivity to the different polarisation states.

Due to the inherent properties of the $gg \to H^* \to ZZ$ and its background, it might be necessary to reconsider the event selection. One possible way to counter the problem of the reduction of $Z_T Z_T$ events in the signal region might be, to employ a discriminant separating $gg \to H^* \to Z_T Z_T$ and $gg \to H^* \to Z_L Z_T$ from the longitudinally polarised events and all of the background.

To further address the issue of the correlating norm factors, it might be advantageous to employ a multi-class DNN to different background processes. That way, the distribution of the sensitive variable might coincide less for background and $gg \to Z_T Z_T$ signal, like it is the case in this analysis.

One problematic aspect remaining is that training a variable that is sensitive to $Z_L Z_T$ and $Z_T Z_T$ contributions can only be trained to discriminate the $Z_L Z_L$ events. Since the contribution of the $Z_L Z_T$ states has a higher number of events, such a variable misses out on a significant part of the sensitivity.

# A. Additional Plots



(a) Control Region
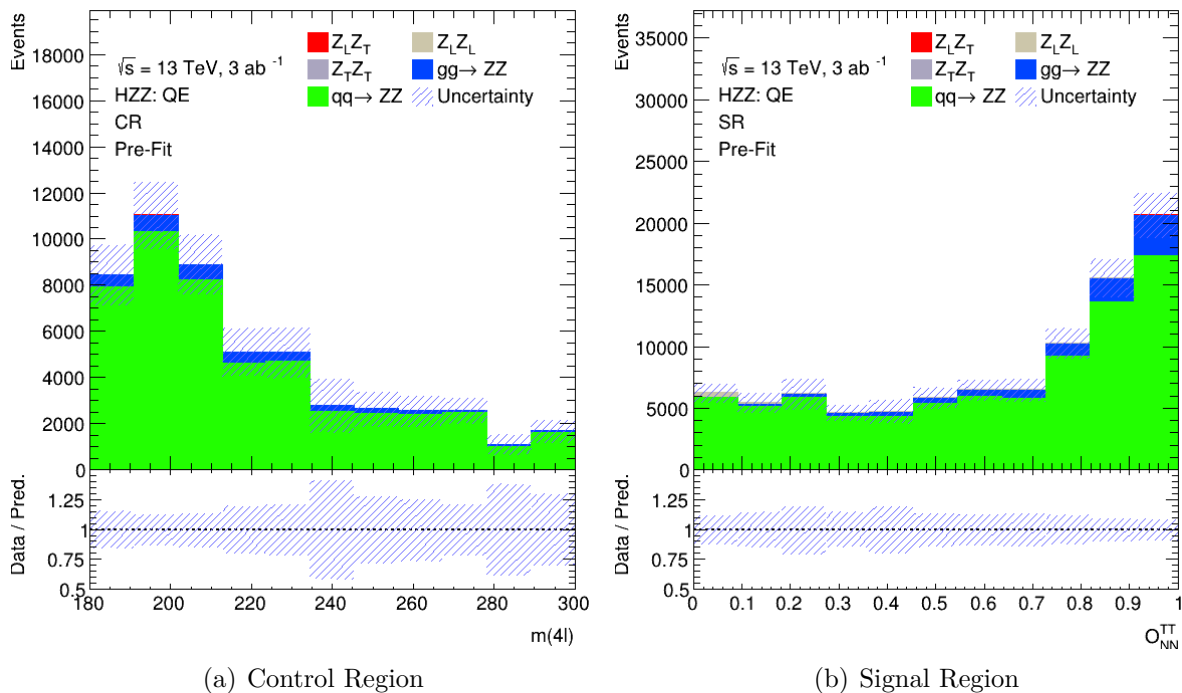
(b) Signal Region

***Figure A.1.:*** Plots of signal and control region with background scaling 1.00.

(a) Control Region
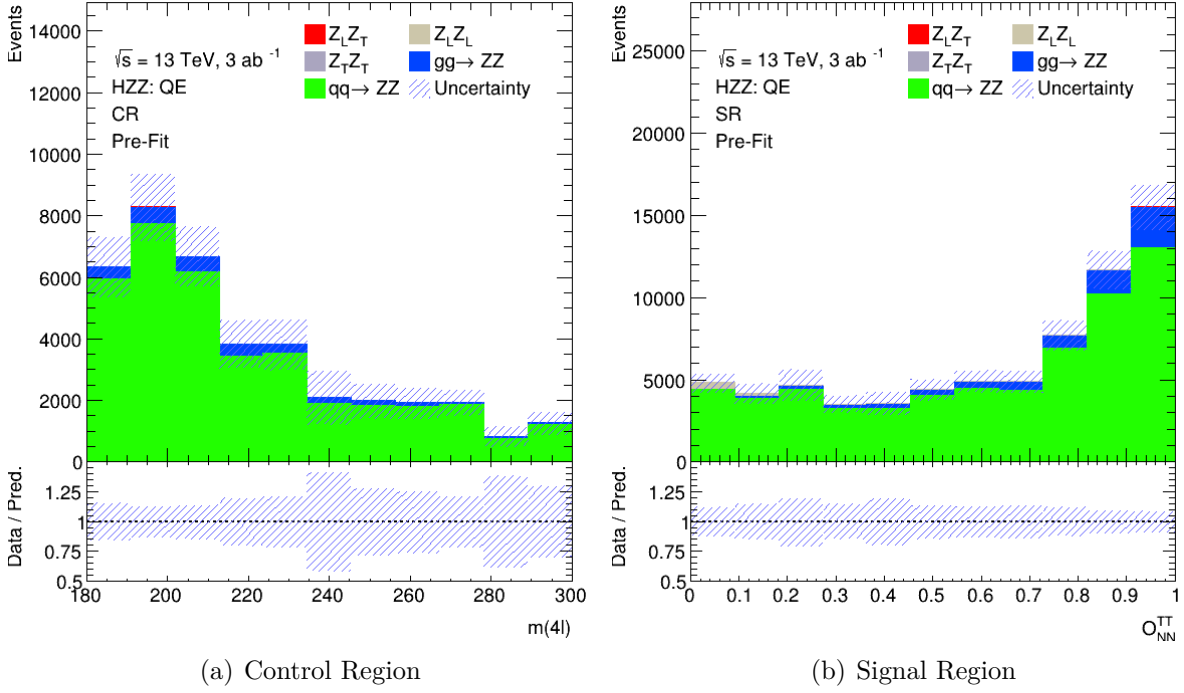
(b) Signal Region

***Figure A.2.:*** Plots of signal and control region with background scaling 0.75.



(a) Control Region
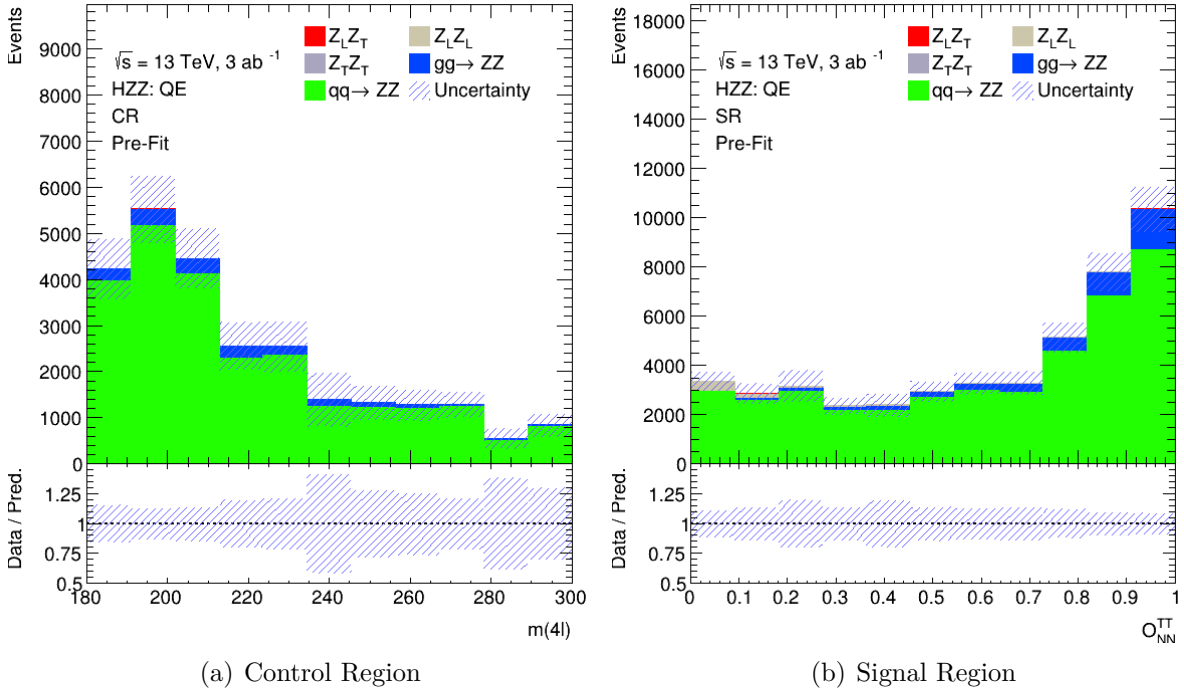
(b) Signal Region

***Figure A.3.:*** Plots of signal and control region with background scaling 0.50.
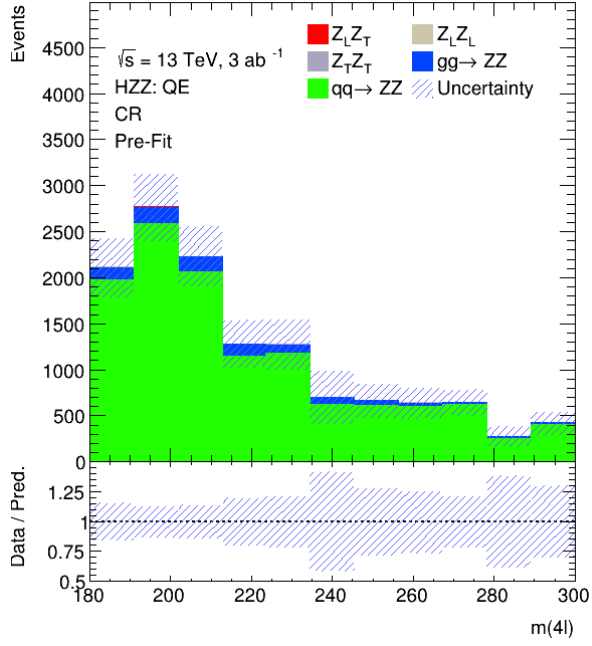
(a) Control Region
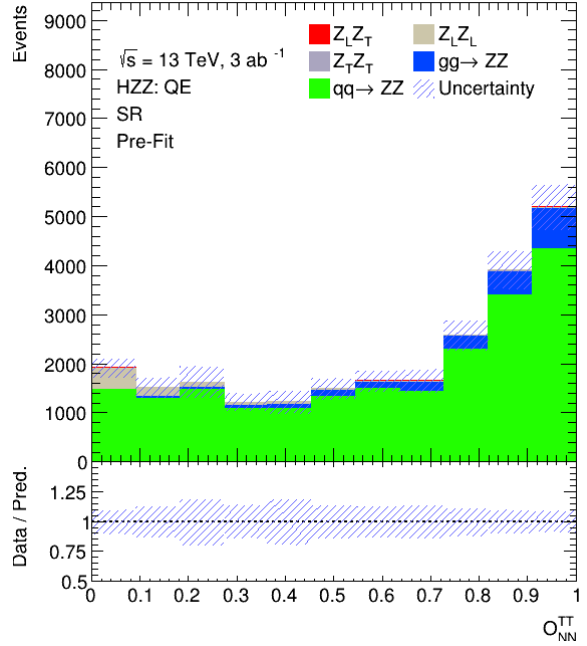
(b) Signal Region

***Figure A.4.:*** Plots of signal and control region with background scaling 0.25.
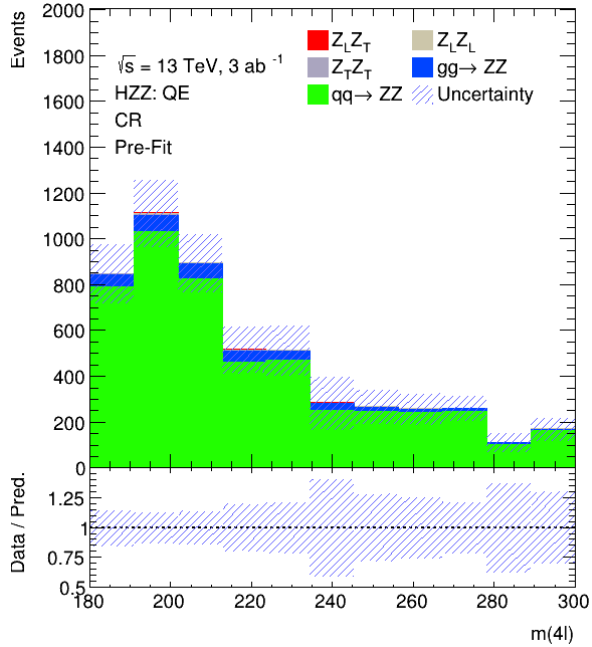


(a) Control Region
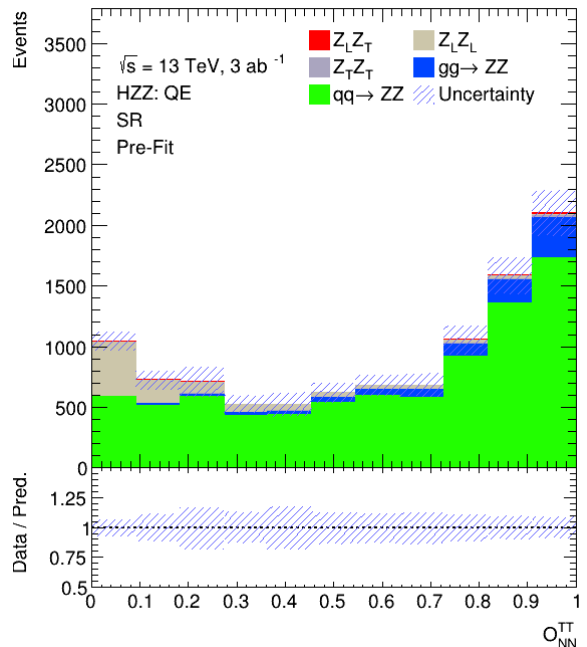
(b) Signal Region

***Figure A.5.:*** Plots of signal and control region with background scaling 0.1.

(a) Control Region
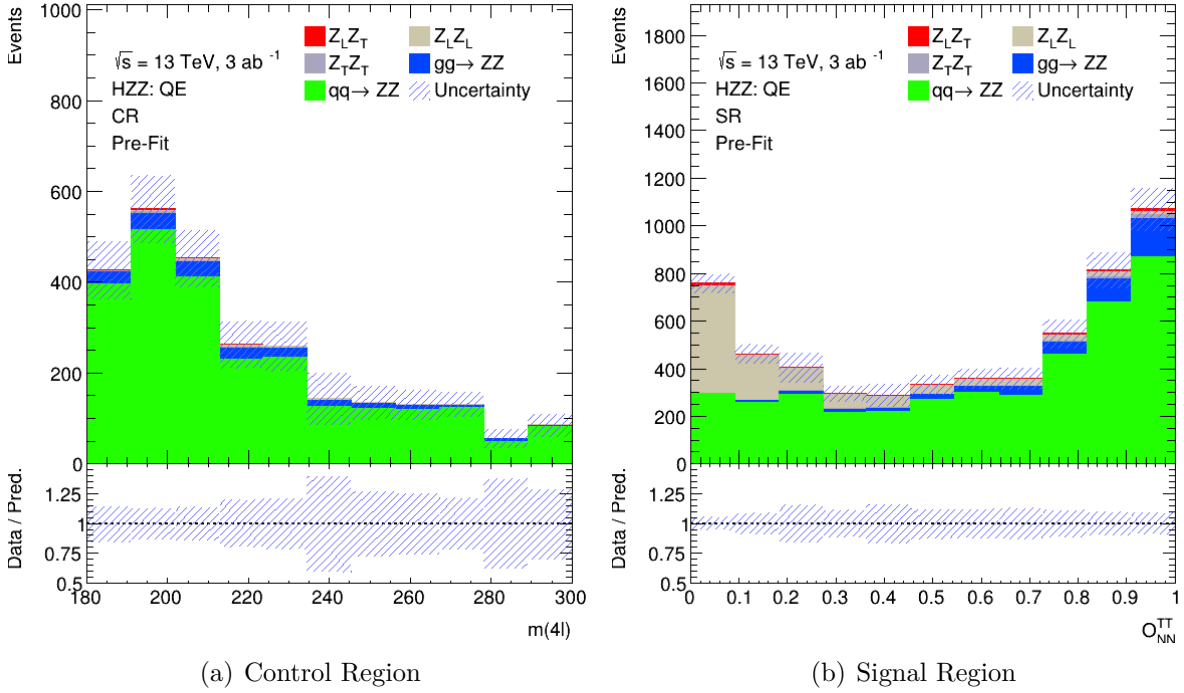
(b) Signal Region

**Figure A.6.:** Plots of signal and control region with background scaling 0.05.



(a) Control Region
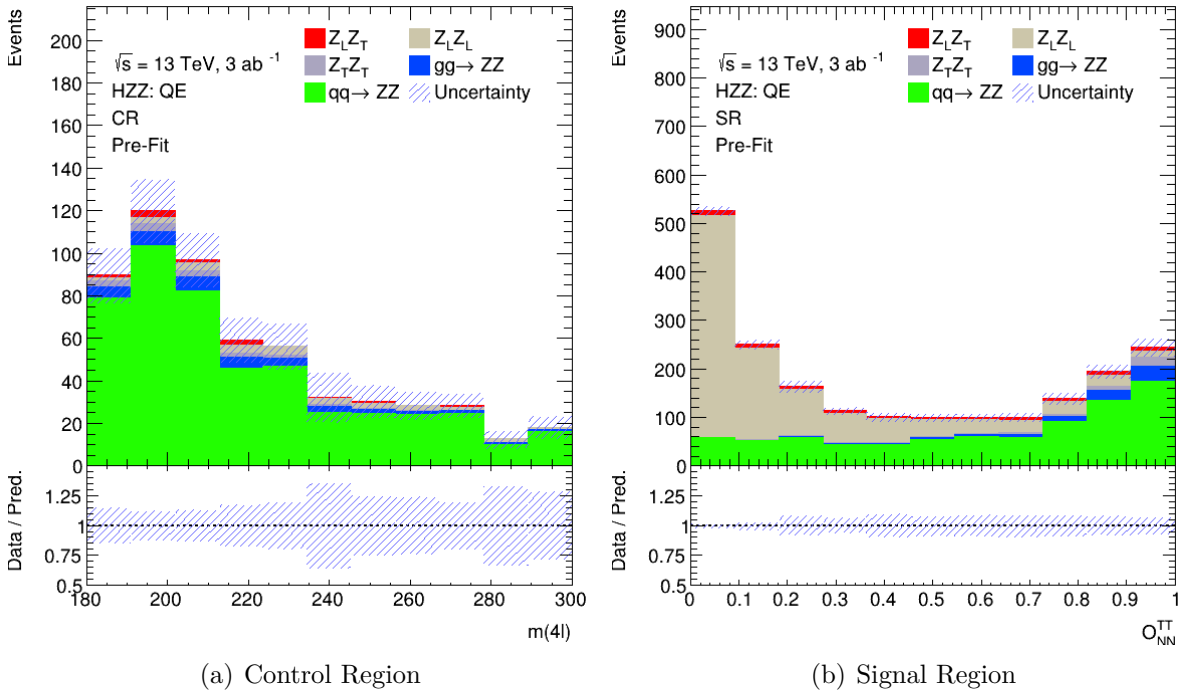
(b) Signal Region

**Figure A.7.:** Plots of signal and control region with background scaling 0.01.
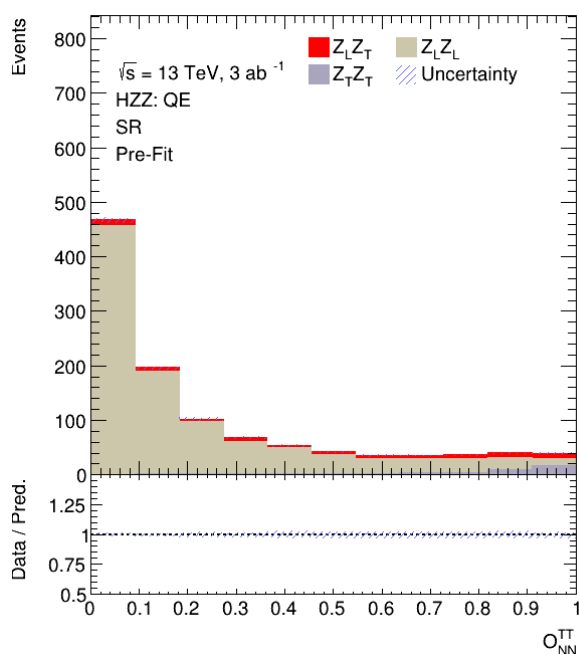
(a) Signal Region

**Figure A.8.:** Plots of signal with background scaling 0.
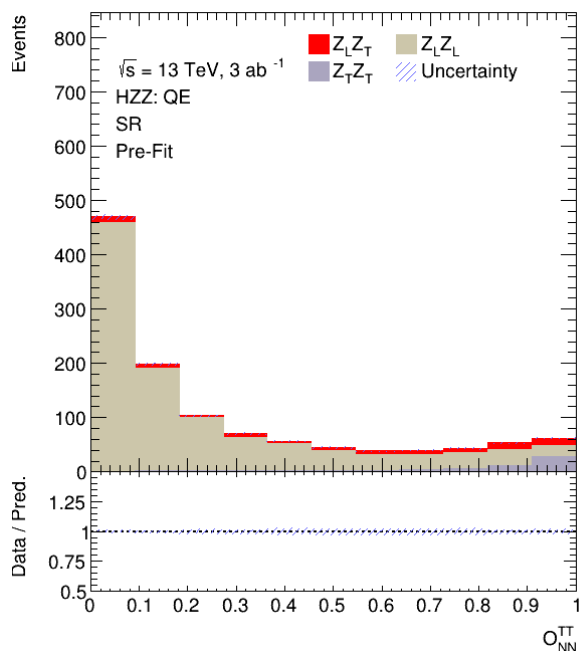


(a) Signal Region

**Figure A.9.:** Plots of signal with only preselection applied.

## A. Additional Plots
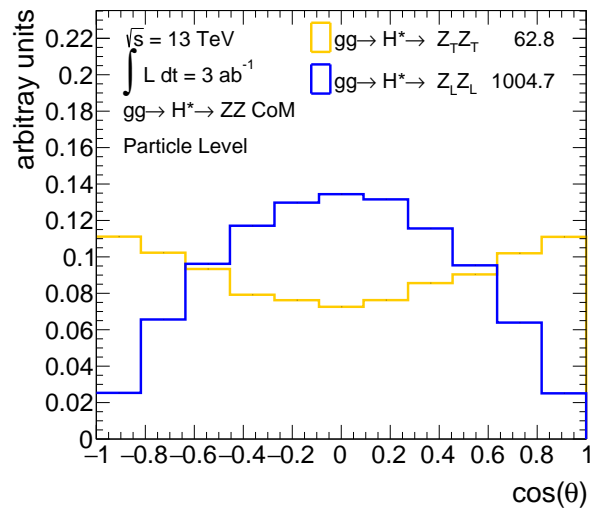


***Figure A.10.:*** $\cos(\theta)$ of the positive lepton emitted by $Z_1$ in the $Z_1$ centre-of-mass frame.
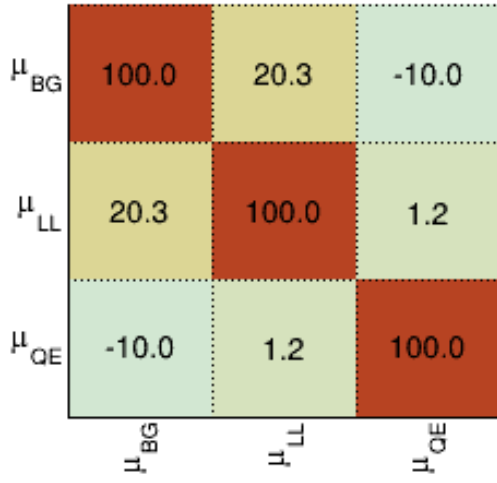
(a) Background scaling 1
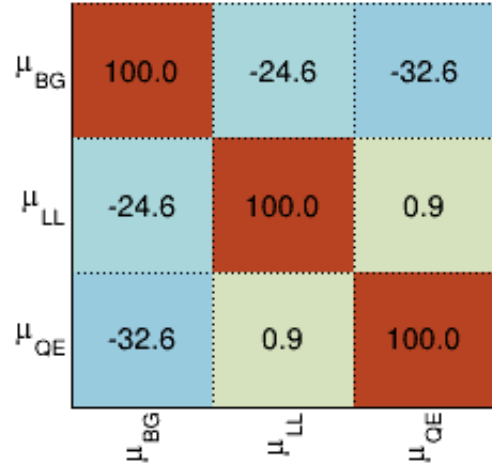
(b) Background scaling 0.75
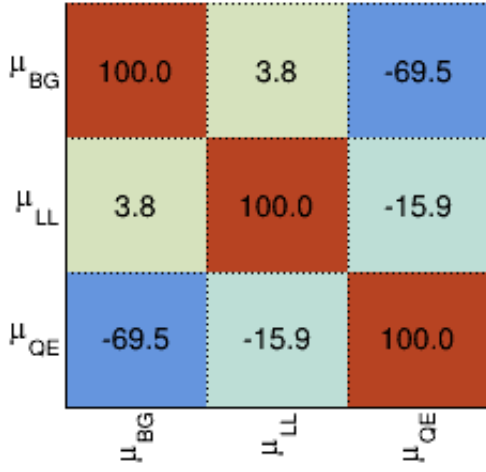
(c) Background scaling 0.5
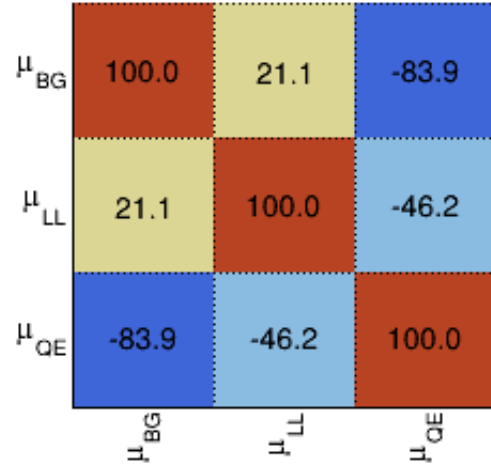
(d) Background scaling 0.25
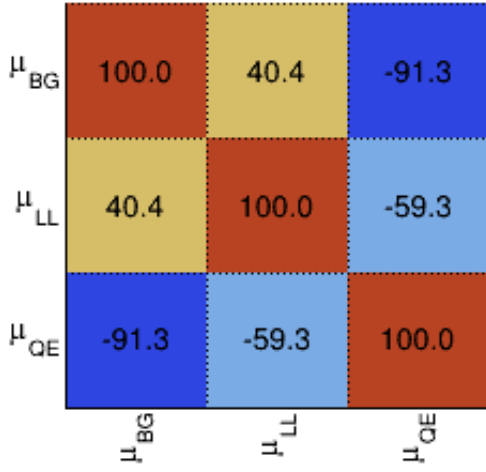
(e) Background scaling 0.10
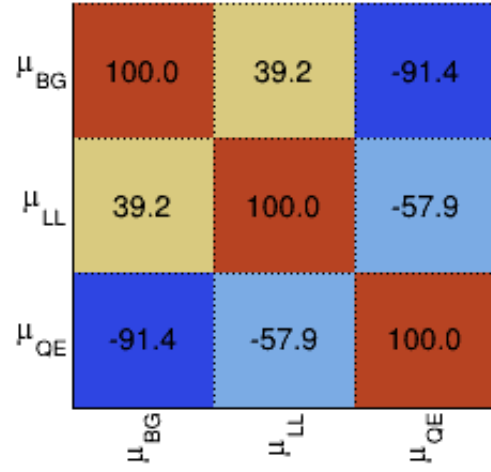
(f) Background scaling 0.05

***Figure A.11.:*** Correlation matrices of the norm factors obtained in the fit for different values of background scaling.

# B. Input Variables



(a) $p_T(\ell_1)$

(b) $p_T(\ell_2)$

(c) $p_T(\ell_3)$

(d) $p_T(\ell_4)$
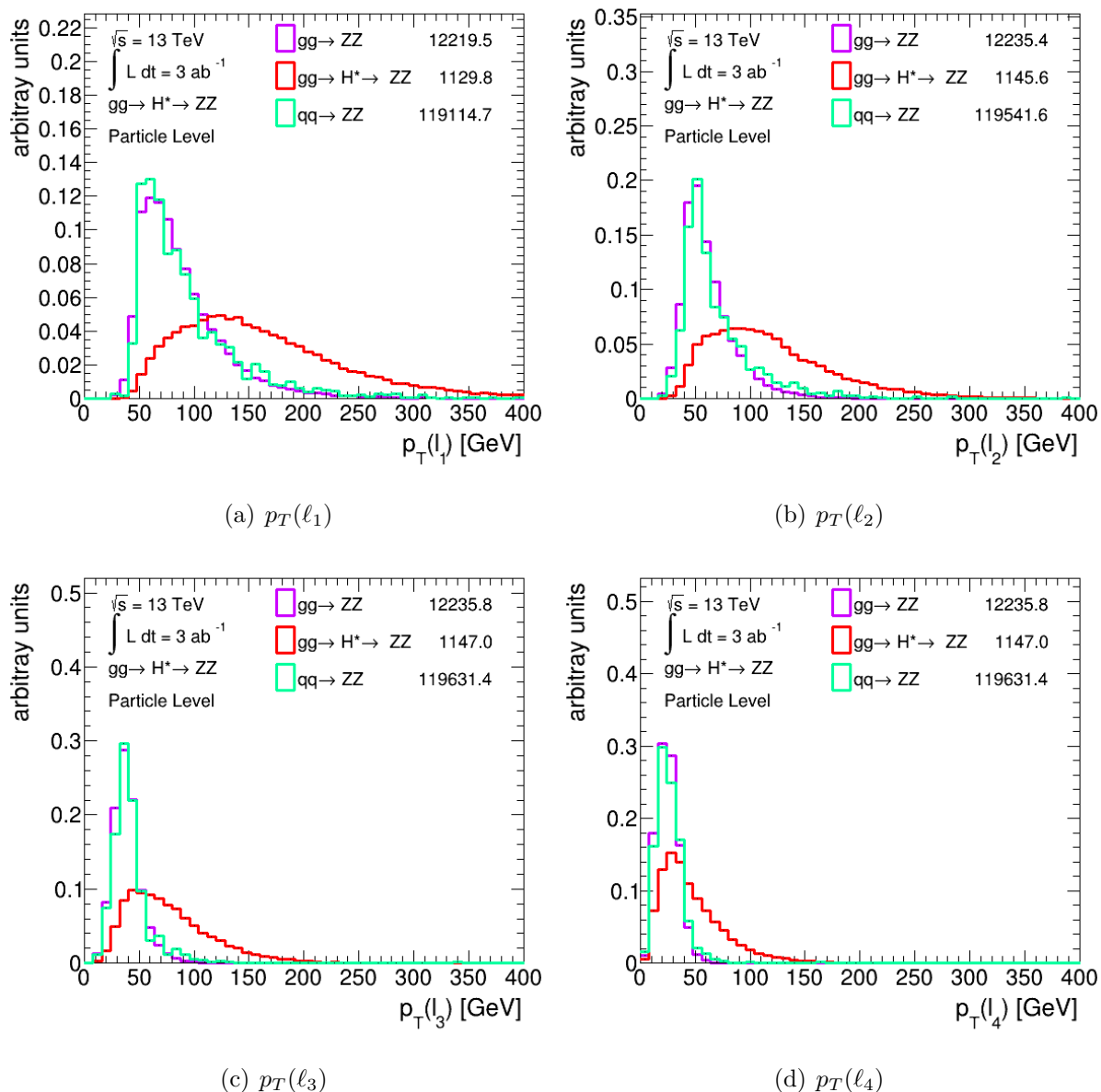
**Figure B.1.:** Distribution of $p_T(\ell_i)$.
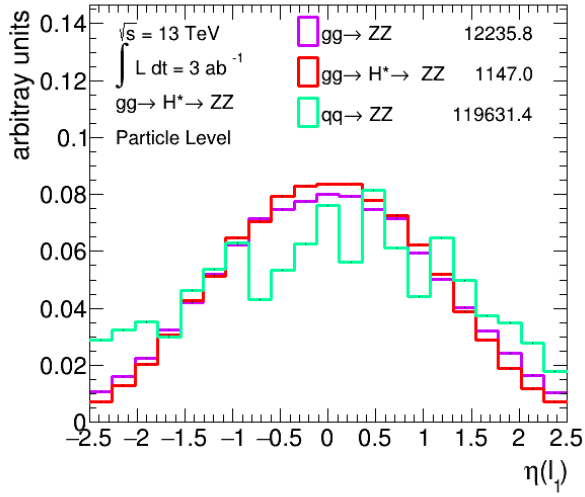
(a) $\eta(\ell_1)$
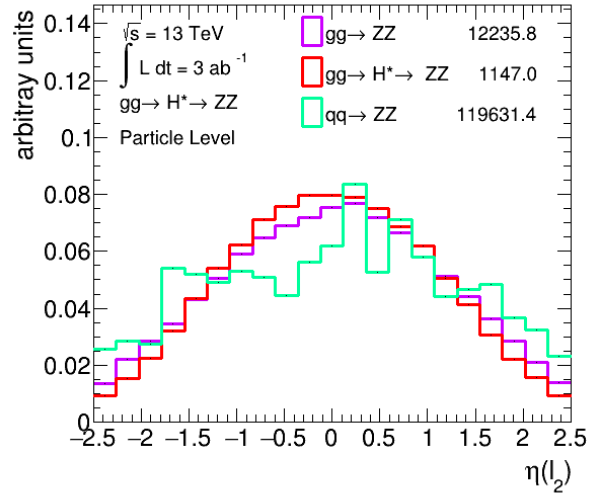


(b) $\eta(\ell_2)$
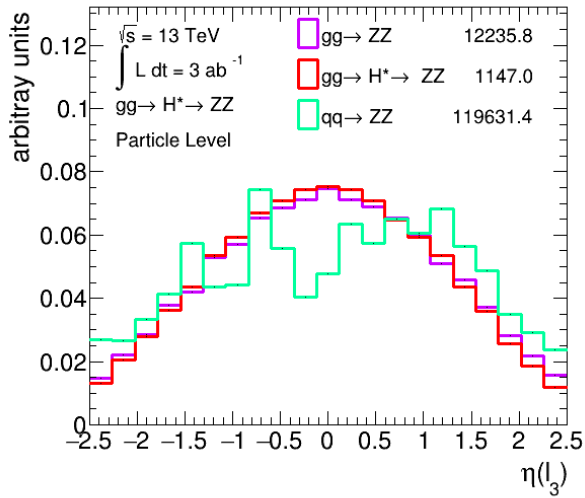


(c) $\eta(\ell_3)$
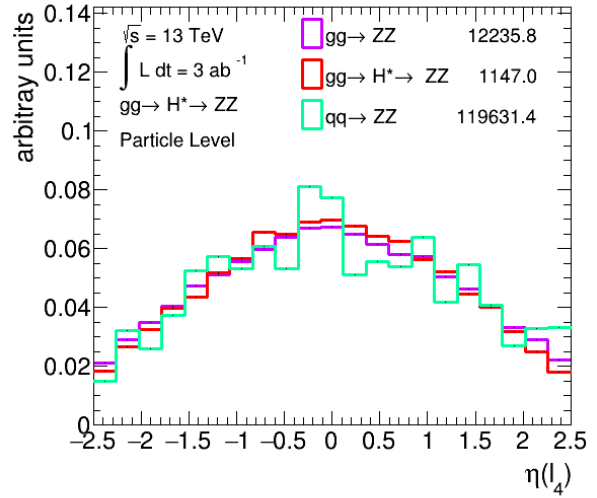


(d) $\eta(\ell_4)$

***Figure B.2.:*** Distribution of $\eta(\ell_i)$.

(a) $E(\ell_1)$
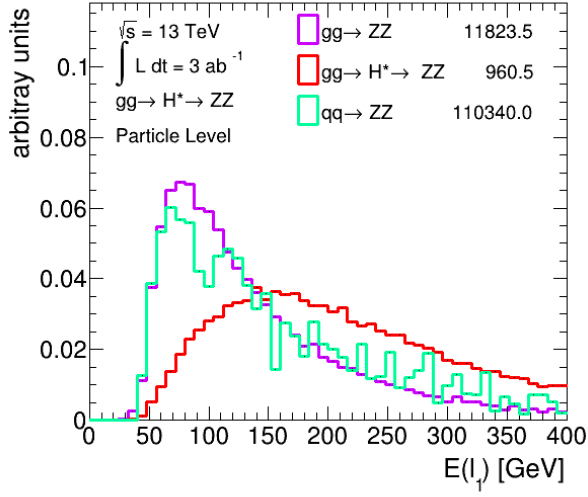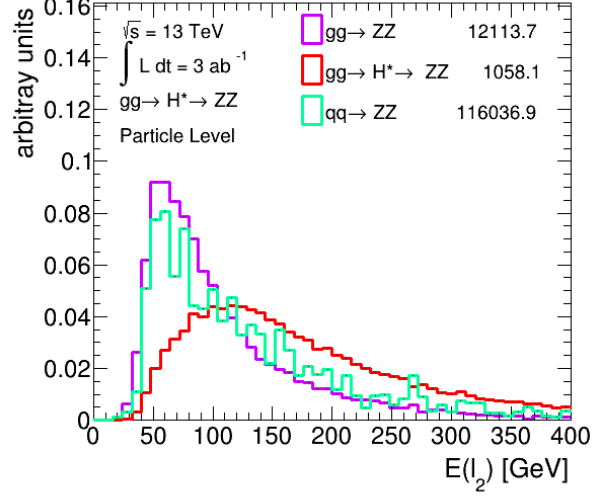
(b) $E(\ell_2)$
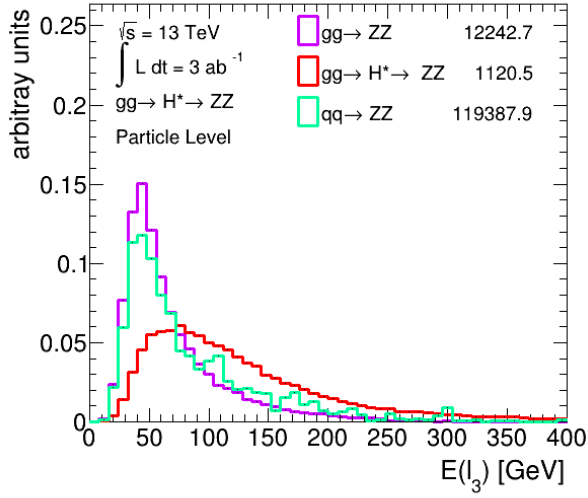
(c) $E(\ell_3)$
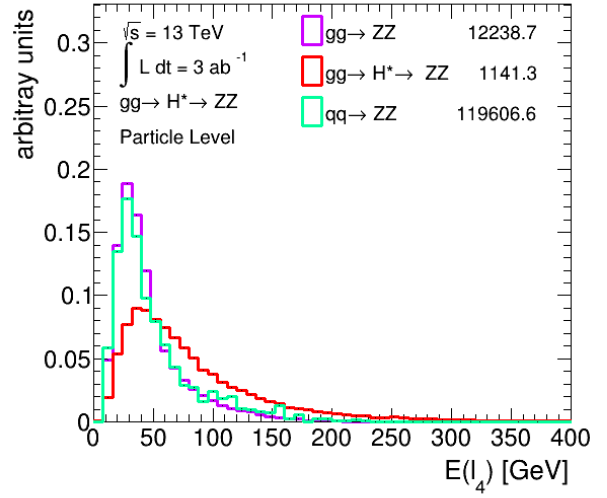
(d) $E(\ell_4)$

**Figure B.3.:** Distribution of $E(\ell_i)$.
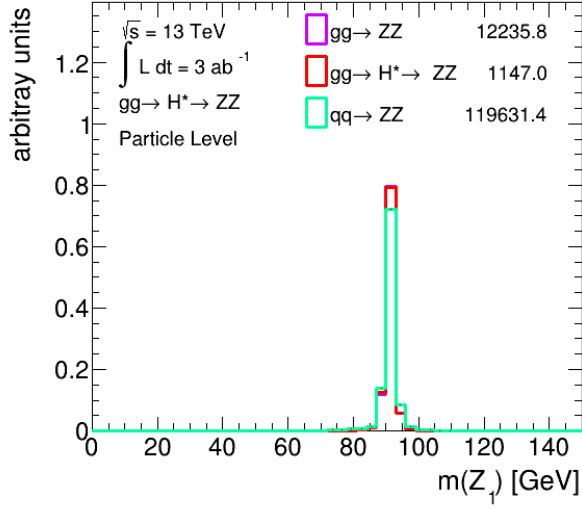
(a) $m(Z_1)$
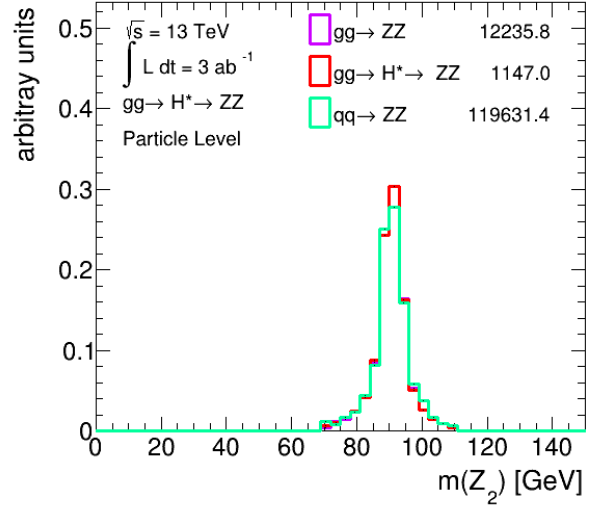
(b) $m(Z_2)$
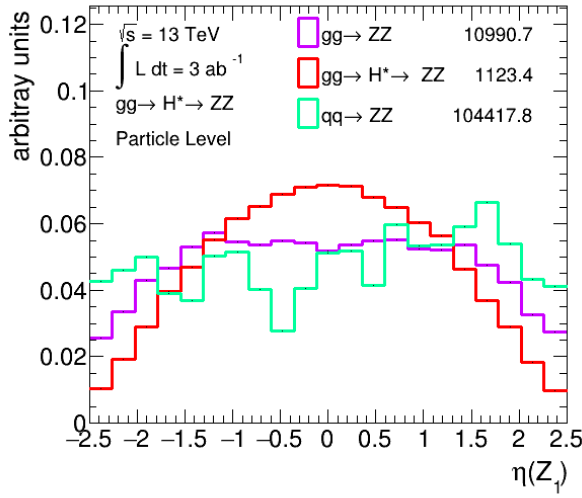


(c) $\eta(Z_1)$
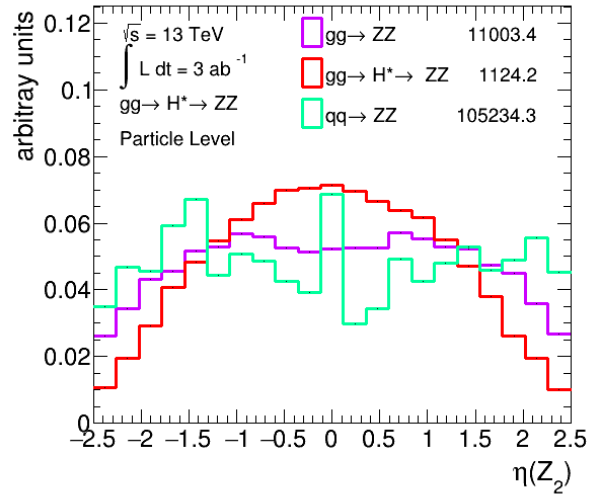
(d) $\eta(Z_2)$

**Figure B.4.:** Distribution of $m(Z_i)$ and $\eta(Z_i)$.
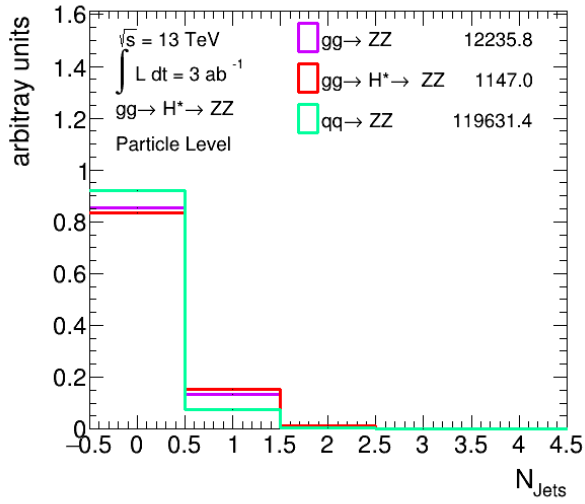
(a) $N_{jets}$
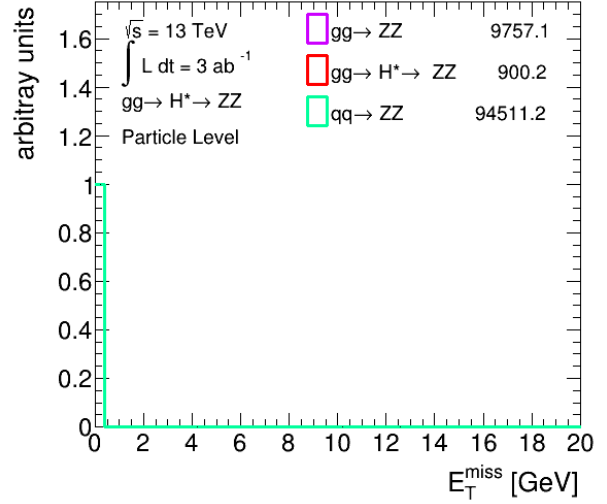
(b) $\cancel{E}_T$
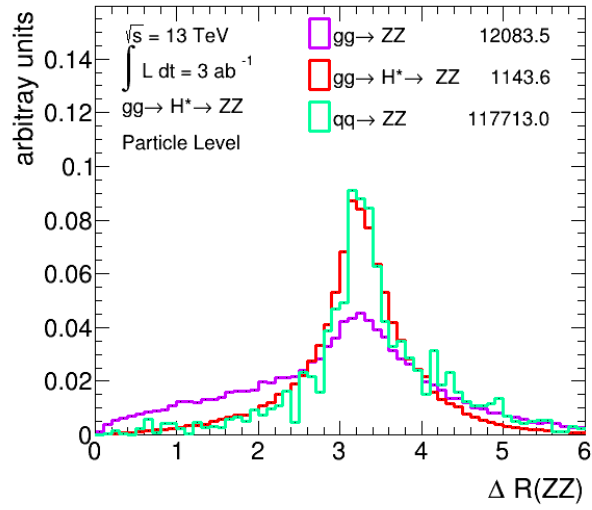


(c) $\Delta R(ZZ)$

**Figure B.5.:** Distribution of $N_{jets}$, $\cancel{E}_T$, and $\Delta R(ZZ)$ .
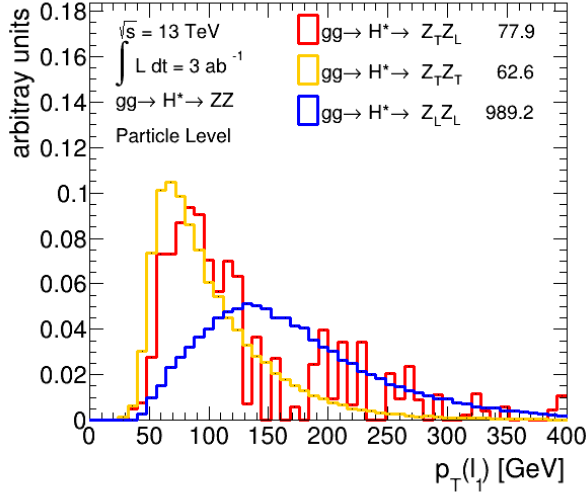
(a) $p_T(\ell_1)$
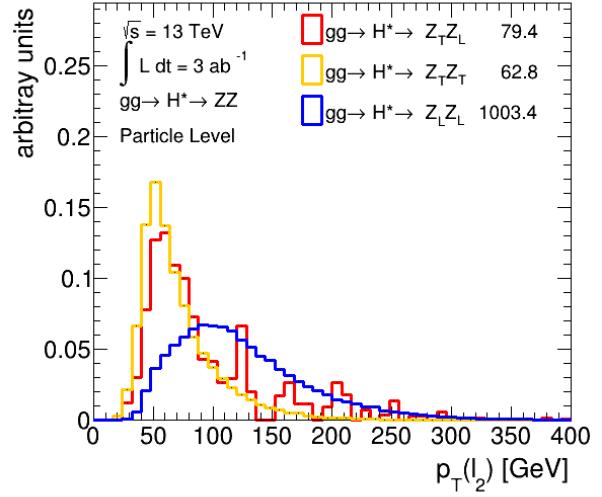
(b) $p_T(\ell_2)$
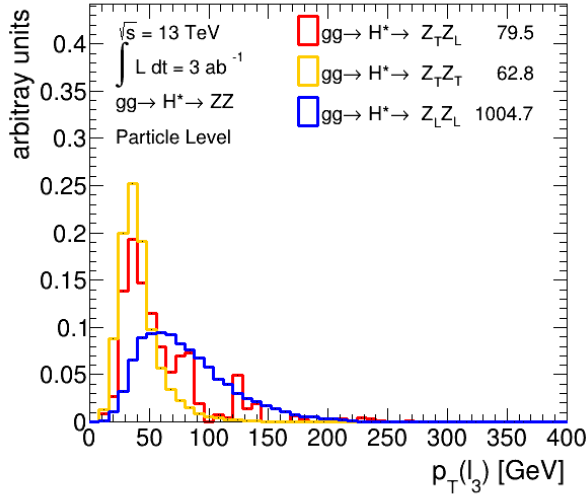


(c) $p_T(\ell_3)$
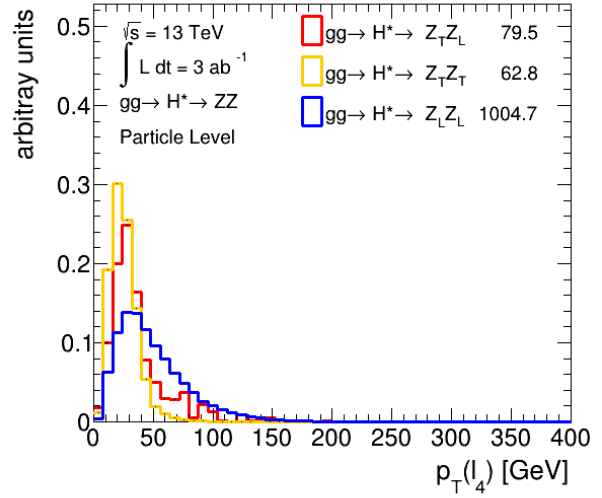
(d) $p_T(\ell_4)$

***Figure B.6.:*** Distribution of $p_T(\ell_i)$.
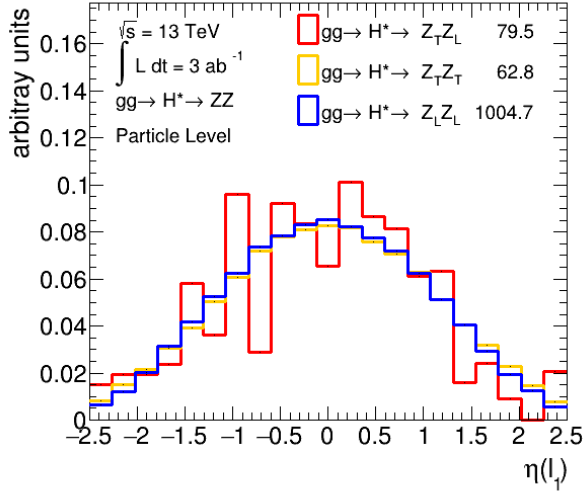
(a) $\eta(\ell_1)$
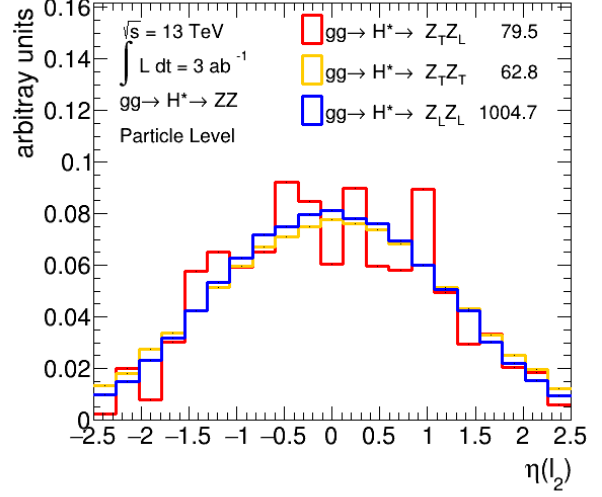
(b) $\eta(\ell_2)$
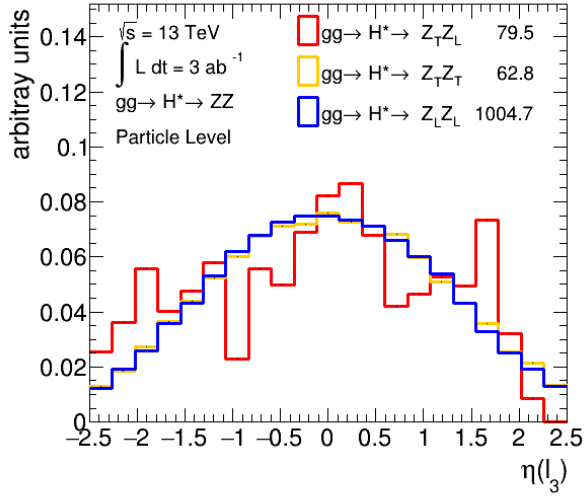
(c) $\eta(\ell_3)$
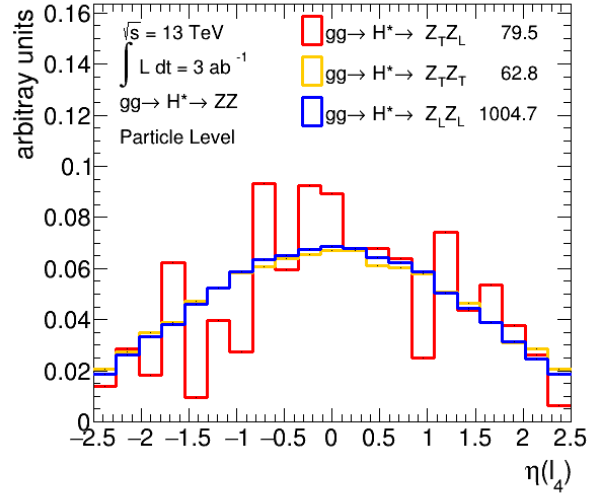
(d) $\eta(\ell_4)$

**Figure B.7.:** Distribution of $\eta(\ell_i)$.

(a) $E(\ell_1)$
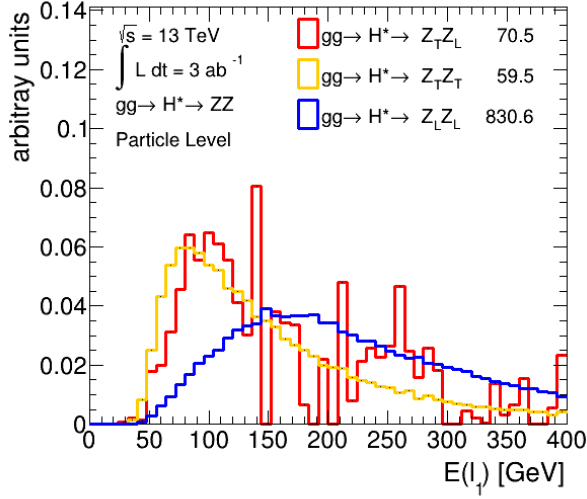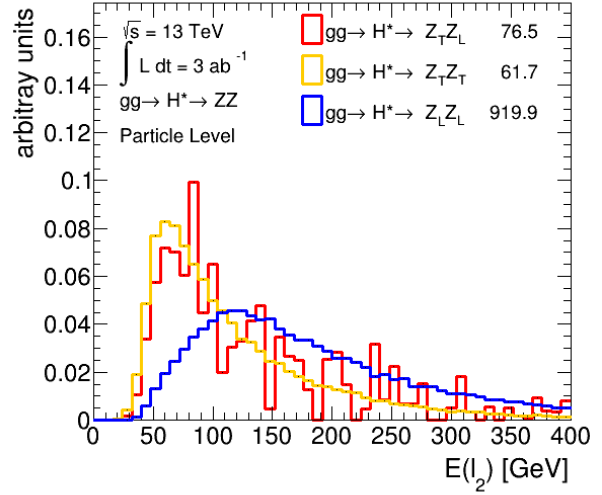
(b) $E(\ell_2)$
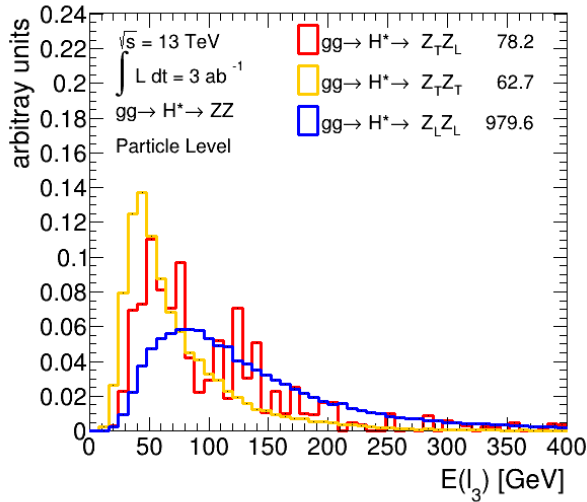
(c) $E(\ell_3)$
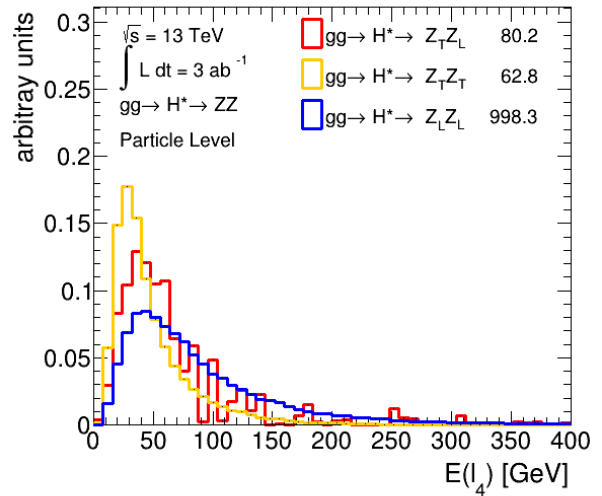
(d) $E(\ell_4)$

**Figure B.8.:** Distribution of $E(\ell_i)$.
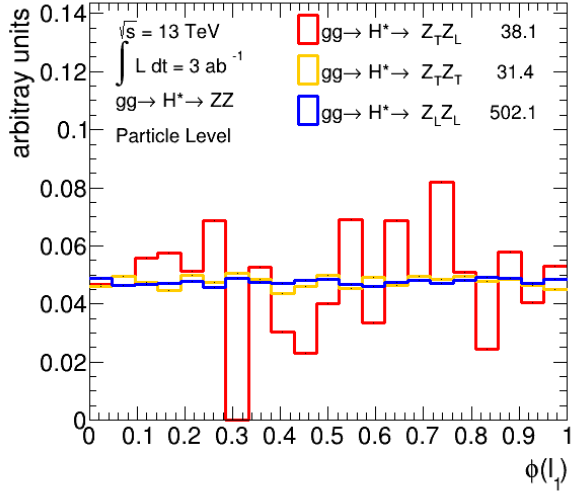
(a) $\phi(\ell_1)$
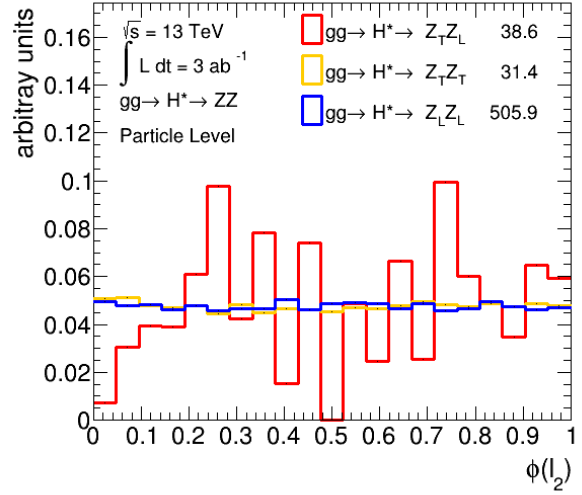
(b) $\phi(\ell_2)$
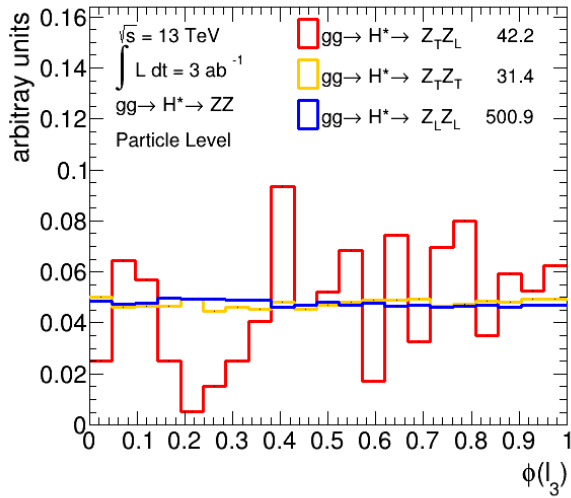
(c) $\phi(\ell_3)$
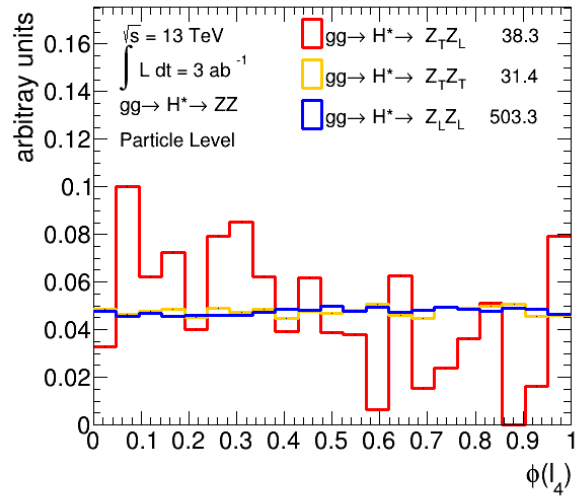
(d) $\phi(\ell_4)$

**Figure B.9.:** Distribution of $\phi(\ell_i)$.

(a) $E(Z_1)$

(b) $E(Z_2)$

(c) CoM $Z_1$ $\eta(\ell^+)$

(d) CoM $Z_2$ $\eta(\ell^+)$

(e) $Z_1$ $\Delta\phi(\ell^+\ell^-)$

(f) $Z_2$ $\Delta\phi(\ell^+\ell^-)$
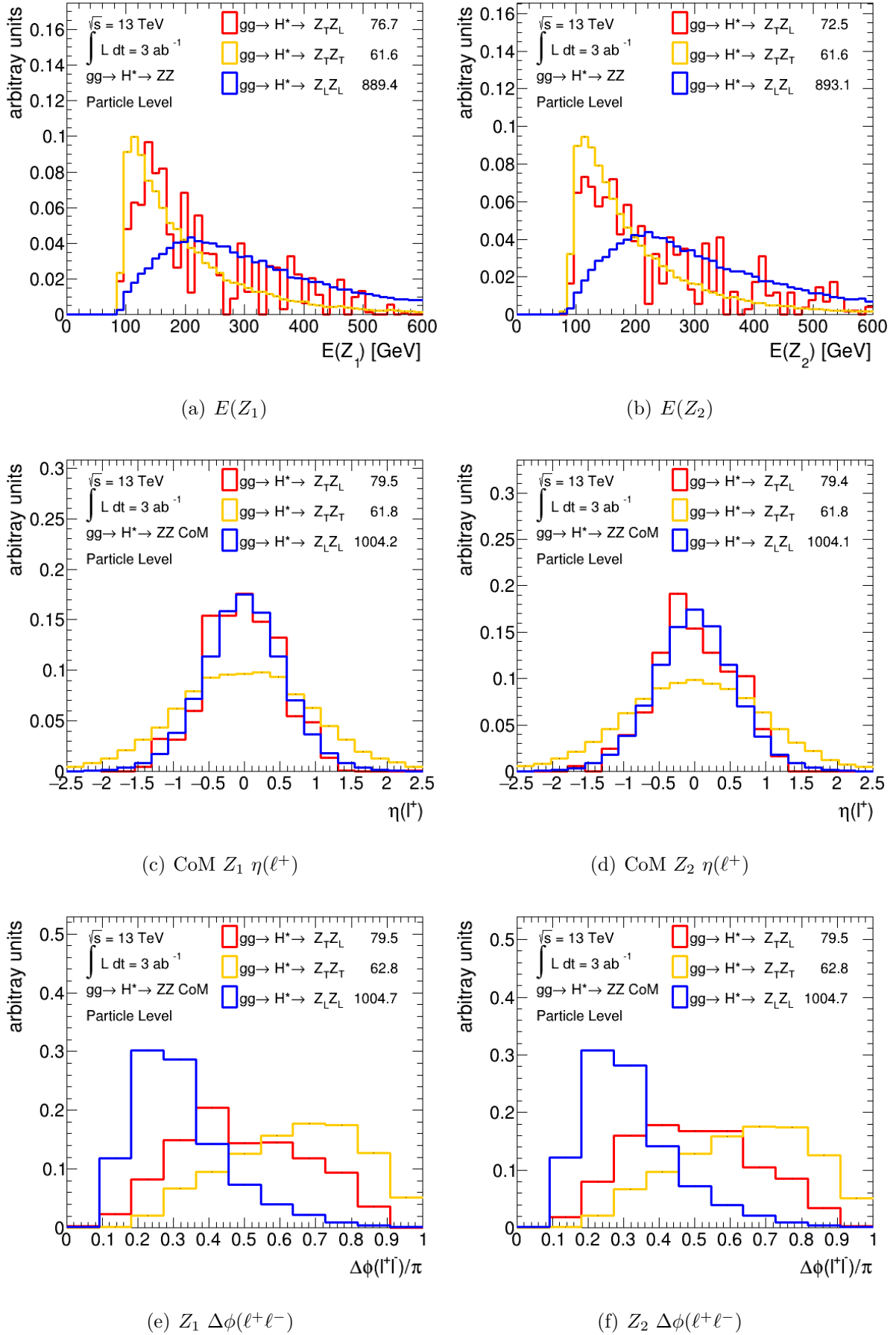
***Figure B.10.:*** Distribution of $E(Z_i)$, CoM $Z_i$ $\eta(\ell^+)$, and $Z_i$ $\Delta\phi(\ell^+\ell^-)$.

# Bibliography

[1] R. L. Workman, et al. (Particle Data Group), *Review of Particle Physics*, PTEP **2022**, 083C01 (2022)

[2] P. W. Higgs, *Broken Symmetries, Massless Particles and Gauge Fields*, Phys. Lett. **12**, 132 (1964)

[3] F. Englert, R. Brout, *Broken Symmetry and the Mass of Gauge Vector Mesons*, Phys. Rev. Lett. **13**, 321 (1964)

[4] P. W. Higgs, *Broken Symmetries and the Masses of Gauge Bosons*, Phys. Rev. Lett. **13**, 508 (1964)

[5] G. S. Guralnik, et al., *Global Conservation Laws and Massless Particles*, Phys. Rev. Lett. **13**, 585 (1964)

[6] P. W. Higgs, *Spontaneous Symmetry Breakdown without Massless Bosons*, Phys. Rev. **145**, 1156 (1966)

[7] T. W. B. Kibble, *Symmetry Breaking in Non-Abelian Gauge Theories*, Phys. Rev. **155**, 1554 (1967)

[8] S. L. Glashow, *Partial Symmetries of Weak Interactions*, Nucl. Phys. **22**, 579 (1961)

[9] S. Weinberg, *A Model of Leptons*, Phys. Rev. Lett. **19**, 1264 (1967)

[10] A. Salam, *Weak and Electromagnetic Interactions*, Almqvist & Wiksell, Stockholm, nobel symposium 8 edition (1968)

[11] S. L. Glashow, et al., *Weak Interactions with Lepton-Hadron Symmetry*, Phys. Rev. D **2**, 1285 (1970)

[12] H. Georgi, et al., *Unified Weak and Electromagnetic Interactions without Neutral Currents*, Phys. Rev. Lett. **28**, 1494 (1972)

*Bibliography*

[13] H. D. Politzer, *Reliable Perturbative Results for Strong Interactions*, Phys. Rev. Lett. **30**, 1346 (1973)

[14] H. D. Politzer, *Asymptotic Freedom: An Approach to Strong Interactions*, Phys. Rept. **14**, 129 (1974)

[15] D. J. Gross, et al., *Asymptotically Free Gauge Theories*, Phys. Rev. D **8**, 3633 (1973)

[16] S. Weinberg, *The Making of the Standard Model*, Eur. Phys. J. C **34**, 5 (2004)

[17] G. 'tHooft, *Renormalization of massless Yang-Mills fields*, Nucl. Phys. B **33(1)**, 173 (1971)

[18] G. 't Hooft, *Renormalizable Lagrangians For Massive Yang-Mills Fields*, Nucl. Phys. B **35**, 167 (1971)

[19] G. 't Hooft, et al., *Regularization And Renormalization Of Gauge Fields*, Nucl. Phys. B **44**, 189 (1972)

[20] G. 't Hooft, et al., *Combinatorics of gauge fields*, Nucl. Phys. B **50**, 318 (1972)

[21] C. Glasman, *Precision measurements of $\alpha_s$ at HERA*, J. Phys. Conf. Ser. **110(2)**, 022013 (2008)

[22] T. Biekötter, et al., *Next-to-next-to-leading order contributions to inclusive jet production in deep-inelastic scattering and determination of $\alpha_s$*, Phys. Rev. D **92**, 074037 (2015)

[23] B. Johannes, et al., *Non-singlet QCD analysis of deep inelastic world data at*, Nucl. Phys. B **774(1-3)**, 182 (2007)

[24] S. Alekhin, et al., *Parton distribution functions, $\alpha_s$, and heavy-quark masses for LHC Run II*, Phys. Rev. D **96(1)**, 014011 (2017)

[25] H. Fritzsch, et al., *Advantages of the color octet gluon picture*, Phys. Lett. **47(4)**, 365 (1973)

[26] M. Gell-Mann, *A Schematic Model of Baryons and Mesons*, Phys. Lett. **8**, 214 (1964)

[27] K. G. Wilson, *Confinement of quarks*, Phys. Rev. D **10**, 2445 (1974)

[28] E. Eichten, et al., *Charmonium: The model*, Phys. Rev. D **17**, 3090 (1978)

[29] D. J. Gross, et al., *Ultraviolet Behavior of Non-Abelian Gauge Theories*, Phys. Rev. Lett. **30**, 1343 (1973)

[30] S. Tomonaga, *On a Relativistically Invariant Formulation of the Quantum Theory of Wave Fields\**, Prog. Theor. Exp. Phys. **1(2)**, 27 (1946)

[31] J. Schwinger, *On Quantum-Electrodynamics and the Magnetic Moment of the Electron*, Phys. Rev. **73**, 416 (1948)

[32] J. Schwinger, *Quantum Electrodynamics. I. A Covariant Formulation*, Phys. Rev. **74**, 1439 (1948)

[33] R. P. Feynman, *Space-Time Approach to Quantum Electrodynamics*, Phys. Rev. **76**, 769 (1949)

[34] R. P. Feynman, *The Theory of Positrons*, Phys. Rev. **76**, 749 (1949)

[35] R. P. Feynman, *Mathematical Formulation of the Quantum Theory of Electromagnetic Interaction*, Phys. Rev. **80**, 440 (1950)

[36] F. J. Dyson, *The Radiation Theories of Tomonaga, Schwinger, and Feynman*, Phys. Rev. **75**, 486 (1949)

[37] F. J. Dyson, *The S Matrix in Quantum Electrodynamics*, Phys. Rev. **75**, 1736 (1949)

[38] C. S. Wu, et al., *Experimental Test of Parity Conservation in Beta Decay*, Phys. Rev. **105**, 1413 (1957)

[39] N. Cabbibo, *Unitary Symmetry and Leptonic Decays*, Phys. Rev. Lett. **10**, 531 (1963)

[40] M. Kobayashi, et al., *CP Violation in the Renormalizable Theory of Weak Interaction*, Prog. Theor. Phys. **49**, 652 (1973)

[41] A. Salam, *Weak and Electromagnetic Interactions*, ed. Nobel Symposium No. 8 (Almqvist & Wiksell, Stockholm, 1968)

[42] ATLAS Collaboration, *Observation of a new particle in the search for the Standard Model Higgs boson with the ATLAS detector at the LHC*, Phys. Lett. B **716**, 1 (2012)

[43] CMS Collaboration, *Observation of a New Boson at a Mass of 125 GeV with the CMS Experiment at the LHC*, Phys. Lett. B **716**, 30 (2012)

[44] J. R. Andersen, et al. (LHC Higgs Cross Section Working Group), *Handbook of LHC Higgs Cross Sections: 3. Higgs Properties* (2013)

*Bibliography*

[45] *Precision electroweak measurements on the Z resonance*, Phys. Rep. **427(5-6)**, 257 (2006)

[46] A. Peres, *Separability Criterion for Density Matrices*, Phys. Rev. Lett. **77**, 1413 (1996)

[47] P. Horodecki, *Separability criterion and inseparable mixed states with positive partial transposition*, Phys. Lett. **232(5)**, 333 (1997)

[48] J. A. Aguilar-Saavedra, et al., *Testing entanglement and Bell inequalities in $H \to ZZ$*, Phys. Rev. D **107**, 016012 (2023)

[49] W. Bernreuther, et al., *A set of top quark spin correlation and polarization observables for the LHC: Standard Model predictions and new physics contributions*, JHEP **2015(12)**, 1 (2015)

[50] R. Rahaman, et al., *Breaking down the entire spectrum of spin correlations of a pair of particles involving fermions and gauge bosons*, Nucl. Phys. B **984**, 115984 (2022)

[51] J. A. Aguilar-Saavedra, *Laboratory-frame tests of quantum entanglement in $H \to WW$*, Phys. Rev. D **107(7)** (2023)

[52] *Luminosity determination in pp collisions at $\sqrt{s} = 13$ TeV using the ATLAS detector at the LHC*, ATLAS-CONF-2019-021 (2019)

[53] ATLAS Collaboration, *High-Luminosity Large Hadron Collider (HL-LHC): Technical design report*, CERN Yellow Reports: Monographs, CERN, Geneva (2020)

[54] ATLAS Collaboration, *The ATLAS Experiment at the CERN Large Hadron Collider*, JINST **3**, S08003 (2008)

[55] U. A. Wiedemann, *HIP and HEP. HIP and HEP*, PoS **ICHEP2020**, 046 (2021)

[56] B. Andersson, et al., *Parton Fragmentation and String Dynamics*, Phys. Rept. **97**, 31 (1983)

[57] T. Sjostrand, *Jet Fragmentation of Nearby Partons*, Nucl. Phys. B **248**, 469 (1984)

[58] B. Webber, *A QCD model for jet fragmentation including soft gluon interference*, Nucl. Phys. B **238(3)**, 492 (1984)

[59] G. Marchesini, et al., *Monte Carlo Simulation of General Hard Processes with Coherent QCD Radiation*, Nucl. Phys. B **310**, 461 (1988)

[60] ATLAS Collaboration, *The ATLAS Simulation Infrastructure*, Eur. Phys. J. C **70**, 823 (2010)

[61] ATLAS Collaboration, *Evidence of off-shell Higgs boson production and constraints on the total width of the Higgs boson in the $ZZ \to 4\ell$ and $ZZ \to 2\ell 2\nu$ decay channels with the ATLAS detector*, Technical report, CERN, Geneva (2022)

[62] J. Alwall, et al., *MadGraph 5: going beyond*, JHEP **2011(6)**, 1 (2011)

[63] E. Bothmann, et al., *Event generation with Sherpa 2.2*, SciPost Phys. **7**, 034 (2019)

[64] D. B. Franzosi, et al., *Automated predictions from polarized matrix elements*, JHEP **2020(4)** (2020)

[65] G. P. Salam, *Towards Jetography*, Eur. Phys. J. C **67**, 637 (2010)

[66] M. Cacciari, et al., *The anti-$k_t$ jet clustering algorithm*, JHEP **04**, 063 (2008)

# Acknowledgement

Looking back at the time and work that led to this thesis, a few persons came to my mind, whose support and encouragement was essential for the outcome of this work. It is utmost important for me, to express my gratitude towards them.

First and foremost, I want to thank Prof. Dr. Arnulf Quadt for giving me the chance to work on this project. Not only did he support and guide me along my way of conducting the research, but he always encouraged me to think more deeply about the physics involved. I also want to thank him for the support in endeavours unrelated to my Bachelor's thesis.

A special thank goes to Prof. Dr. Ariane Frey, who not only was my second referee, but with her interesting particle physics lecture helped to keep my interest in physics alive, even during the darkest hours.

Another person without whom this work would not have been possible, is Dr. Baptiste Ravina. His guidance and wisdom in any matter of physics was of great importance to me when preparing this thesis.

Stephen Eggebrecht was always the first in line to be confronted with my questions, whether it was related to physics, programming or something else. I am thankful, that he patiently and competently answered even my most trivial questions.

Aside from those named already, I want to thank all the members of the data analysis meeting group of Prof. Quadt. The fruitful discussions have been very insightful for me. Even though, it cost me a few of my lunch breaks, it was time very well spent.

Last but not least I want to thank all my friends keeping me company in the "Glaskasten". I am very grateful for your support. I know that times have been very stressful and I was not always easy to deal with, but I am thankful that you supported me no matter what. I can not think of a better group of friends to have around me.

**Erklärung** nach §13(9) der Prüfungsordnung für den Bachelor-Studiengang Physik und den Master-Studiengang Physik an der Universität Göttingen: Hiermit erkläre ich, dass ich diese Abschlussarbeit selbständig verfasst habe, keine anderen als die angegebenen Quellen und Hilfsmittel benutzt habe und alle Stellen, die wörtlich oder sinngemäß aus veröffentlichten Schriften entnommen wurden, als solche kenntlich gemacht habe.

Darüberhinaus erkläre ich, dass diese Abschlussarbeit nicht, auch nicht auszugsweise, im Rahmen einer nichtbestandenen Prüfung an dieser oder einer anderen Hochschule eingereicht wurde.

Göttingen, den 3. September 2023

(Siemen Aulich)